The size and pervasiveness of Ly α-UV spatial offsets in star-forming galaxies at z ~ 6

Lemaux, B.C.; Fuller, S.; Bradač, M.; Pentericci, L.; Hoag, A.; Strait, V.; … ; Pforr, J.

Note: To cite this publication please use the final published version (if applicable).

The Size and Pervasiveness of Lyα-UV Spatial Offsets in Star-Forming Galaxies at $z \sim 6$

B. C. Lemaux [1]★, S. Fuller [1], M. Bradač [1], L. Pentericci [2], A. Hoag [3],
V. Strait [1], T. Treu [3], C. Alvarez[4], P. Bolan[1] , P. J. Gandhi[1] , K.-H. Huang [1],
T. Jones [1], C. Mason [5,6], D. Pelliccia [1,7], B. Ribeiro [8], R. E. Ryan [9],
K. B. Schmidt [10], E. Vanzella [11], Y. Khusanova [12,13], O. Le Fèvre [13],
L. Guaita [2,14], N. P. Hathi [9], A. Koekemoer [9], J. Pforr [15] (Affiliations are listed at the end of the paper)

ABSTRACT

We study the projected spatial offset between the ultraviolet continuum and Lyα emission for 65 lensed and unlensed galaxies in the Epoch of Reionization ($5 \leq z \leq 7$), the first such study at these redshifts, in order to understand the potential for these offsets to confuse estimates of the Lyα properties of galaxies observed in slit spectroscopy. While we find that ~40% of galaxies in our sample show significant projected spatial offsets ($|\Delta_{Ly\alpha-UV}|$), we find a relatively modest average projected offset of $|\widetilde{\Delta}_{Ly\alpha-UV}| = 0.61\pm0.08$ proper kpc for the entire sample. A small fraction of our sample, ~10%, exhibit offsets in excess of 2 proper kpc, with offsets seen up to ~4 proper kpc, sizes that are considerably larger than the effective radii of typical galaxies at these redshifts. An internal comparison and a comparison to studies at lower redshift yielded no significant evidence of evolution of $|\Delta_{Ly\alpha-UV}|$ with redshift. In our sample, UV-bright galaxies ($\widetilde{L_{UV}}/L_{UV}^* = 0.67$) showed offsets a factor of three greater than their fainter counterparts ($\widetilde{L_{UV}}/L_{UV}^* = 0.10$), 0.89±0.18 vs. 0.27±0.05 proper kpc, respectively. The presence of companion galaxies and early-stage merging activity appeared to be unlikely causes of these offsets. Rather, these offsets appear consistent with a scenario in which internal anisotropic processes resulting from stellar feedback, which is stronger in UV-brighter galaxies, facilitate Lyα fluorescence and/or backscattering from nearby or outflowing gas. The reduction in the Lyα flux due to offsets was quantified. It was found that the differential loss of Lyα photons for galaxies with average offsets is not, if corrected for, a limiting factor for all but the narrowest slit widths (<0.4″). However, for the largest offsets, if they are mostly perpendicular to the slit major axis, slit losses were found to be extremely severe in cases where slit widths of ≤1″ were employed, such as those planned for *James Webb Space Telescope*/NIRSpec observations.

Key words: galaxies: evolution – galaxies: high-redshift – galaxies: reionization – gravitational lensing: strong – techniques: spectroscopic – techniques: photometric

1 INTRODUCTION

The advent of ground-based 8-10-*m* class telescopes such as the Very Large Telescope array (VLT), Keck, Gemini, and Subaru, extremely sensitive ground-based sub-millimeter arrays such as the Atacama Large Millimeter/submillimeter Array (ALMA), as well as space-based optical/near-infrared facilities such as the *Hubble* Space Telescope (*HST*) and the *Spitzer* Space Telescope, performing imaging and spectroscopy at a variety of wavelengths have

enabled studies of galaxies at increasingly higher redshifts. These studies, especially those over the last decade, have now become powerful enough to begin to explore the epoch known as "reionization" (EoR), during which the first stars, galaxies, and active galactic nuclei (AGN) were beginning to ionize what was a neutral intergalactic medium of hydrogen gas (e.g., Treu et al. 2013; Tilvi et al. 2014, 2020; Schmidt et al. 2016; Hashimoto et al. 2019b, 2018, 2019a; Mason et al. 2018, 2019; Hoag et al. 2019b; Tamura et al. 2019; Fuller et al. 2020; Pelliccia et al. 2021). It is expected that the very first galaxies started to form when the universe was less than 1 Gyr old (see, e.g., Mawatari et al. 2020; Strait et al. 2020

★ E-mail: blemaux@ucdavis.edu

and references therein), i.e., at $z \gtrsim 6$, and that these first sources played a crucial role in the reionization that appears to have ended at z~6 (Becker et al. 2001; Fan et al. 2006). Such a timescale is consistent with observations of the Cosmic Microwave Background from the *Planck* telescope, which use the Thomson optical scattering depth to infer the epoch of an instantaneous reionization at $7.0 \lesssim z \lesssim 8.5$ (Planck Collaboration et al. 2016, 2020). While admirable attempts have been made to find and characterize galaxies formed during the EoR through large imaging and spectroscopic campaigns performed in blank fields, as well as around massive clusters of galaxies to harness the power of gravitational lensing, observational constraints, especially from a spectroscopic perspective, still remain sparse. At the highest redshifts, such campaigns are just now gaining the power to seriously challenge theoretical models of galaxy formation. Unsurprisingly, these galaxy populations remain a key driver of future instrumentation and major missions such as the *James Webb Space Telescope* (*JWST*; Gardner et al. 2006), the *Nancy Roman Grace Space Telescope* (Spergel et al. 2015), the Thirty Meter Telescope (TMT; Sanders 2013), Giant Magellan Telescope (GMT; Johns et al. 2012), and the Extremely Large Telescope (ELT; Gilmozzi & Spyromilio 2007).

The identification of high-redshift star-forming galaxies is often done through the $n = 2 \rightarrow n = 1$ Lyα λ1216Å transition of hydrogen (hereafter Lyα). Lyα emission primarily originates from the recombination of ionized hydrogen around newly-formed stars that emit large amounts of ionizing radiation. Lyα emission can be extremely strong as it is intrinsically the brightest recombination line (Partridge & Peebles 1967) and is situated well into the rest-frame UV. As such, Lyα is, in principle, easily detected at very high redshifts, giving it large potential as a tool for high-redshift galaxy evolution and cosmological studies. Other rest-frame UV lines such as CIV λ1549Å, HeII λ1640Å, and CIII] λ1907,1909Å are seen relatively rarely, are generally too faint, and, when bright, likely originate from galaxy populations too biased to particular phases, such as during the presence of AGN, to serve as a reliable, general substitute for Lyα line emission (e.g., Cassata et al. 2013; Schmidt et al. 2016; Nakajima et al. 2018; Le Fèvre et al. 2019, though see Stark et al. 2015a,b for an alternative view). While considerable headway has been made in measuring the [OIII] 88μm and [CII] 158μm emission lines in high-redshift ($z \gtrsim 4$) galaxies primarily from the ALMA or the (Extended) Very Large Array (VLA) (e.g., Ferkinhoff et al. 2010; Capak et al. 2015; Inoue et al. 2016; Pentericci et al. 2016; Bradač et al. 2017; Carniani et al. 2017; Le Fèvre et al. 2020; Béthermin et al. 2020), most detected galaxies are required to have a redshift from rest-frame UV spectroscopy prior to their targeting, as blind surveys for these lines are expensive (though see, e.g., Smit et al. 2018; Hashimoto et al. 2018; Zhou et al. 2020; Loiacono et al. 2021 for counterexamples).

Lyα emission is strongest when the ionizing stars are numerous, young, and an appreciable amount of atomic gas remains either *in situ* or in close proximity. However, Lyα photons scatter resonantly, which creates numerous complications for its ability to escape the emitting galaxy, the circumgalactic medium, and the surrounding neutral intergalactic medium (IGM, e.g., Peebles 1993; Dijkstra 2014). These complications are compounded immensely in presence of dust in the interstellar medium (ISM) of galaxies, which serves to absorb Lyα photons during the resonant scattering process (e.g., Dayal et al. 2011; Hayes et al. 2011; Cassata et al. 2015) and leads to an expected decline in the observed fraction of Lyα-emitters (LAEs) at a fixed equivalent width (*EW*) limit with decreasing redshift. The reverse trend is expected at $z \gtrsim 6$ due to the presence of

an increasingly neutral IGM, such as that during reionization the fraction of LAEs again at a fixed *EW* limit should decrease with increasing redshift. The confluence of these two effects appears to lead to a picture where the fraction of LAEs increases from $z \sim 0$ until the edge of the reionization era ($z \sim 6$) and then begins to drop precipitously at higher redshifts. Such a trend is indeed observed when the fraction of LAEs or derivative Lyα quantities have been used to probe the physical conditions during the reionization epoch, with such studies pointing to evidence of an increasingly neutral medium at $z \gtrsim 6$ (e.g., Ota et al. 2008; Fontana et al. 2010; Pentericci et al. 2011, 2018b; Ono et al. 2012; Treu et al. 2013; Schenker et al. 2014; Tilvi et al. 2014; Hu et al. 2017; Zheng et al. 2017; Hoag et al. 2019b; Mason et al. 2018, 2019; Fuller et al. 2020, though see, e.g., De Barros et al. 2017; Caruana et al. 2018; Kusakabe et al. 2020 for a slightly different view). The fractional amount of Lyα estimated to escape star-forming galaxies can also be used to place constraints on internal galaxy physics (e.g., Dijkstra et al. 2011; Hayes et al. 2011; De Barros et al. 2017; Sobral et al. 2018) and the measured velocity difference between the Lyα feature and the systemic velocity as well as the Lyα line profile can be used to constrain kinematic models of such galaxies (e.g., Dawson et al. 2002; Westra et al. 2005; Sawicki et al. 2008; Verhamme et al. 2008, 2015; Schaerer & Verhamme 2008; Steidel et al. 2010; Dijkstra 2014; Guaita et al. 2017; Marchi et al. 2019; Cassata et al. 2020). Additionally, various Lyα properties may be helpful in indicating the amount of ionizing photons escaping galaxies (e.g., Dijkstra et al. 2016; Verhamme et al. 2017; Marchi et al. 2018; Steidel et al. 2018; Mason & Gronke 2020), a key element of reionization models.

While such properties make Lyα an extremely useful tool for probing the physics of high-redshift galaxies and of reionization, it is also an extremely frustrating one. Without the presence of Lyα, or the other few emission lines that are detectable at high-redshift given observational and temporal constraints, the veracity of photometric redshift estimates cannot be determined. That Lyα does not appear in emission for the majority of galaxies at all redshifts blunts its effectiveness as a tool to confirm redshifts. While mitigating measures involving the full photometric redshift probability density function, $P(z)$, in conjunction with other constraints can be used even when Lyα is not present (e.g., Mason et al. 2018; Hoag et al. 2019b; Mason et al. 2019; Fuller et al. 2020), other, more subtle issues remain with the Lyα feature.

Early investigations of the spatial size of Lyα emission using *HST* data (e.g., Finkelstein et al. 2011), ground-based narrowband imaging (e.g., Steidel et al. 2011), and predictions from simulations (e.g., Zheng et al. 2011) all indicated that Lyα sizes might exceed those in the rest-frame UV. This has now been confirmed, as studies of large numbers of galaxies at $3 \lesssim z \lesssim 6$ observed with integral field unit (IFU) spectroscopy from the Keck Cosmic Web Imager (KCWI; Morrissey et al. 2018) and the Multi-Unit Spectroscopic Explorer (MUSE; Bacon et al. 2010, 2014) have clearly demonstrated that, on average, Lyα halo sizes of LAEs well exceed their UV extent, with typical size ratios of ~3-10 (e.g., Wisotzki et al. 2016, 2018; Leclercq et al. 2017; Erb et al. 2018). Such differences are not limited only to sizes; in local analogs of high-redshift star-forming galaxies, Lyα emission exibits differences from rest-frame UV emission in a variety of morphological measures (Guaita et al. 2015). Additionally, recent work on large samples of LAEs over a similar redshift range ($2 \lesssim z \lesssim 5$) observed with slit spectroscopy from the Very Large Telescope array (VLT) have shown that galaxies can exhibit non-negligible spatial offsets in their Lyα emission relative to that of their rest-frame UV continuum (Hoag et al. 2019a),

with large offsets (∼ 2 proper kpc) observed in 10-20% of star-forming galaxies near the characteristic UV luminosity, ∼ L^*_{UV}, at $z \gtrsim 2$ (Ribeiro et al. 2020). These studies confirm earlier work on single galaxies or narrowband imaging observations of large samples of LAE candidates, of the existence of a class of LAE with large, significant Lyα-UV spatial offsets (Bunker et al. 2000; Fynbo et al. 2001; Shibuya et al. 2014). Both the larger extent of the Lyα emitting region and the spatial offset from the rest-frame UV continuum location would lead to additional losses of Lyα flux in observations relying on slit spectrographs, as slits are typically placed on the UV barycenter and slit widths are typically much smaller than the observed Lyα halo size. If Lyα halo sizes or spatial offsets were a strong function of redshift or of other physics related to the galaxy populations or their surrounding media, such effects could have severe impacts on the inference of galaxy properties and the evolution of the IGM during the EoR.

In this paper, we study the latter of these two effects, the projected Lyα-UV spatial offset, in a sample of 36 high-redshift ($5 \lesssim z \lesssim 7$) lensed LAEs taken from Fuller et al. (2020) and 29 high-redshift non-lensed LAEs drawn from Pentericci et al. (2011) and Pentericci et al. (2018b). This represents the first such study performed on a large sample of galaxies at this redshift. Due in part to lensing, the combined galaxy sample spans more than three orders of magnitude in intrinsic UV brightness, which allows for a comparison of offsets in UV-brighter and UV-fainter samples. Additionally, we compare to the few samples available in the literature at $2 \lesssim z \lesssim 5$ for which this measurement has been made. The paper is structured as follows. In §2 we present the samples used in this study, the associated data, and the process of measuring various quantities including the Lyα-UV offset for both our magnified and unmagnified sample. In §3 we discuss the relationship between the Lyα-UV offset and other properties of the galaxies including redshift, discuss the possible genesis for these offsets, and quantify the amount of additional slit loss resulting from these offsets for a variety of observational setups. §4 presents our conclusions.

Throughout this paper all magnitudes are presented in the AB system (Oke & Gunn 1983; Fukugita et al. 1996) and distances are given in proper rather than comoving units. We adopt a concordance ΛCDM cosmology with $H_0 = 70$ km s^{-1} Mpc^{-1}, $\Omega_\Lambda = 0.73$, and $\Omega_M = 0.27$. While abbreviated for convenience, throughout the paper absolute magnitudes are in units of $M_{AB} + 5 \log(h_{70})$, luminosities in units of h_{70}^{-2} ergs s^{-1}, and proper distances and volumes in units of h_{70}^{-1} kpc and h_{70}^{-3} Mpc^3, respectively, where $h_{70} \equiv H_0/70$ km^{-1} s Mpc. All equivalent widths are given in the rest-frame.

2 DATA AND ANALYSIS

In this section we present both sets of high-redshift LAEs used in this paper as well as the measurements of various quantities that enter into our analysis, which include the estimate of spatial offsets between the observed Lyα feature and the rest-frame UV continuum. It is important to note here that, since we are observing these galaxies with slit spectroscopy instead of, e.g., integral field unit spectroscopy, we can only constrain those offsets which occur along one-dimension, namely that parallel to the major axis of the slit. Thus, all offsets presented here are projected offsets in this dimension implying they are necessarily lower limits, as is the frequency of significant offsets. While we use the term "spatial offset" throughout the paper, we ask the reader to keep in mind that we always refer to the projected offset.

2.1 Magnified Sample

The majority of our magnified sample is drawn from the sample presented in Fuller et al. (2020). This sample includes 36 LAEs[1] observed over the redshift range $5 \lesssim z \lesssim 7$, each lensed by a massive foreground cluster. These LAEs were compiled from a massive, ∼200 hour[2] spectroscopic campaign with the DEep Imaging Multi-Object Spectrograph (DEIMOS; Faber et al. 2003) situated at the right Nasmyth focus of the Keck II telescope. In total, 10 cluster fields were targeted with Keck/DEIMOS. These clusters include four of the five *Hubble* Frontier Fields (HFFs; Abell et al. 1989; Ebeling et al. 2001; Lotz et al. 2017), several clusters from the Cluster Lensing And Supernova survey with Hubble (CLASH; Postman et al. 2012), and other efficient lensing clusters with comparable data from the Spitzer UltRa Faint SUrvey Program (SURF-SUP; Bradač et al. 2014). Each cluster was observed with the Advanced Camera for Surveys (ACS; Ford et al. 1998) and the Wide Field Camera 3 (WFC3; MacKenty et al. 2008) aboard the *Hubble* Space Telescope (*HST*) in a large complement of broadband filters to a depth of ∼27-29 per filter. In addition, all clusters were imaged with the non-cryogenic bands of the *Spitzer* Space Telescope InfraRed Array Camera (IRAC; Fazio et al. 2004) to 3σ depths of $m_{AB} \sim 26 - 27$ per filter (Ryan et al. 2014; Bradač et al. 2014; Huang et al. 2016; Lotz et al. 2017). These imaging data were used to select high-redshift candidate objects through a series of color-color and photometric redshift (hereafter z_{phot}) cuts for spectroscopic targeting with Keck/DEIMOS. In addition, potential high-redshift line emitters observed in the Grism Lens-Amplified Survey from Space (GLASS; Schmidt et al. 2014, 2016; Treu et al. 2015) survey were also selected and prioritized as targets. High-redshift candidates were targeted, in addition to arcs and potential cluster members (referred to broadly as "filler slits"), with multi-object slitmasks to a depth ranging from an exposure time, τ_{exp} of 3480s-19200s across all masks ($\langle \tau_{exp} \rangle \sim 7800$s). Slit widths of 1″ were used for all observations. Note that, in many cases, high-redshift candidates appeared on multiple masks (see Fuller et al. 2020 for more details). In all such cases, the spectrum from each individual mask was used to constrain the various parameters used in this study and an error-weighted sum was used to obtain the final values for each candidate.

At the completion of the observing campaign, a final high-redshift candidate sample of 198 objects was compiled in Fuller et al. (2020). This final sample relied on a uniform criterion involving the likelihood of the galaxy being in a redshift window that made the observation of the Lyα feature possible. Additionally, a systematic search was performed for high-redshift candidates that were serendipitously subtended by one or several of the observed slits. A semi-automated search of the one-dimensional signal-to-noise spectra of both targeted and serendipitous high-z candidates resulted in a final sample of 36 LAEs. All 36 of these LAEs had both visual emission line detections and formal line significances typically well in excess of 3σ. The median spectroscopic redshift of the 36 LAEs in our sample is $\bar{z}_{spec} = 6.23$ and the redshift distribution of these galaxies is shown in the left panel of Figure 1. A more complete account of the observations, reduction, and analysis of these data are given in Fuller et al. (2020).

---

[1] While not all galaxies in our sample have *EW*s in excess of the traditional limit used to define LAEs (i.e., 20-25Å), we adopt this term for simplicity.
[2] Note that this number refers to the total time spent on the telescope rather than the sum of the DEIMOS integration time, which is roughly 100 hours.

2.1.1 *Lyα Spatial centroids of the Magnified Sample*

To measure the Lyα[3] location of the LAEs from Fuller et al. (2020) we collapsed the two-dimensional spectrum over the wavelength range where the Lyα emission appears in excess of the background. In the observed-frame this width was typically ~8Å. Note that this procedure was done for each individual night that a LAE was observed and the resultant values were combined for a given galaxy by a weighted average of all observations, where the signal-to-noise ratio (S/N) of the Lyα line in each observation is used as the weight. Prior to a formal measurement of the Lyα location, because the two-dimensional DEIMOS slits reduced through the SPEC2D package have an ambiguity in their directionality, which, in turn, results in an ambiguity in the cardinal direction of any observed offset, we measured the distance from the southern edge of the slit[4] to the rest-frame UV location of the target in each slit. This distance was then compared to the design location encoded by DSIMULATOR[5], the DEIMOS mask design software (see §2.1.2 for more details on DSIMULATOR). Coincident values meant the two-dimensional spectrum was oriented such that increasing pixel values along the major axis of the slit corresponded to more northerly movement[6], discordant values meant the slit was flipped, and increasing pixel values along the major axis of the slit resulted in movement southward.

Once the spectrum was collapsed and the orientation determined, we used two methods to attempt to determine the spatial centroid of the Lyα emission. The first and most common method used was to fit a Gaussian to the collapsed one-dimensional spatial profile of the Lyα emission through a χ^2-minimization technique using the IDL-based package MPFITEXPR. The errors in each case were derived from the official SPEC2D inverse-variance spectrum. The mean of the Gaussian fit was adopted as the raw[7] spatial centroid and the associated uncertainties were taken from the covariance matrix. The second method, which was used only in a small percentage (~15%) of cases where the S/N was generally too low or artifacts prevented a clean Gaussian fit, relied on the non-parametric approach of Teague & Foreman-Mackey (2018). Briefly, this approach identifies the pixel value where the collapsed spectrum is at maximum and uses this value, along with the value of the two directly adjacent pixels, to estimate the curvature of the spatial profile on either side of the maximum. A quadratic function then uses this input to estimate the line centroid. In essentially all high S/N cases where spectra were devoid of strong artifacts, the two methodologies returned similar results within the errors.

Because of the ability of differential atmospheric refraction (DAR) to alter the spatial location at which an object is seen at different wavelengths, the measurement of Lyα location must either occur in close spectral proximity to the rest-frame ultraviolet (UV)

continuum measurement (i.e., similar wavelengths) or a correction must be applied to account for this effect. In the case where the continuum is present in the spectra, this issue is obviated with a continuum measurement just redward of the Lyα feature, as indeed was done for our unmagnified sample (see §2.2). In the case of our magnified sample, however, little to no continuum is observed, requiring a correction for this effect. In the next section, we will estimate the spatial location of the UV continuum at the central wavelength of each mask (8800Å for the vast majority of our data). As such, we corrected the raw Lyα spatial location to that expected at the central wavelength of the mask it is observed on using the method described in Appendix A.

2.1.2 *Rest-frame UV Spatial centroids of the Magnified Sample*

Because of the absence of the continuum in the spectral observations of the magnified sample, we are required to estimate the rest-frame UV location of these galaxies based on its expected location from DSIMULATOR. Note that a few galaxies, especially those which serendipitously fell on the slit (see Appendix A), were not centered along the minor axis of the slit and, thus, the expected UV position was also a projected one. This expected location is based on the right ascension and declination (α, δ) of each target and corrected for the effect of DAR *at the central wavelength of a given mask* using the expected airmass and position angle (PA) relative to the parallactic angle of the observation, values which are input by the user at the time of the mask design. Because the actual observations are taken at a variety of airmass and PAs, typically over the course of many nights, the true DAR correction will be different than the one expected from the values input during the mask design process. In Appendix A we quantify the magnitude of this effect and the estimate of the UV centroid for LAE candidates that were serendipitously subtended by our slits. Additionally, we also discuss in Appendix A potential scatter in our measurements due to relative astrometric errors and conclude that such uncertainties are small enough to be ignored.

At the end of this process described in Appendix A, we have estimates of the rest-frame UV and Lyα pixel locations corrected for DAR and mask design issues. These two estimates are subtracted, the absolute value is taken, and the resultant number is multiplied by the DEIMOS spatial plate scale ($0.1185'' \text{ pix}^{-1}$) and the angular scale at the redshift of the LAE to get the main quantity used in this analysis: $|\Delta_{Ly\alpha-UV}|$ in units of proper kpc (pkpc). Since all galaxies in this sample are lensed, we make the simple assumption here that the galaxy is enlarged with azimuthal symmetry and the true distance measured is given as $|\Delta_{Ly\alpha-UV}| \equiv |\Delta_{Ly\alpha-UV}|_{lensed}/\sqrt{\mu}$, where μ is the magnification of each galaxy as estimated by the formalism of Bradač et al. (2005, 2009). For more detail on the lensing reconstruction for the fields studied here see Hoag et al. (2019b) and references therein. In Figure 2 we show examples drawn from our full sample of strong Lyα emission offset at both a typical and extreme level from the UV continuum emission.

The vast majority of the galaxies in our sample have relatively small magnification factors ($\mu \lesssim 5$). Therefore, the validity of the above assumption is of limited consequences for our results and, indeed, our main results remain unchanged if we do not assume the magnification is azimuthally symmetric and, instead, assume a variety of different ellipticities. This logic applies as well to our ignorance of the true magnification, an ignorance which is present both within the confines of a given model as well as the variation in the recovered values for different modeling approaches. For the former, the formal uncertainties within our own models of the

---

[3] While there remains some ambiguity as to the nature of the emission line, as discussed in Fuller et al. (2020), the possibility that these galaxies are genuine LAEs is very high. Therefore, we refer to this line simply as Lyα for the remainder of the paper.

[4] No slits had sky PAs of 90° or 270°, which meant the "southern edge of the slit" was always a defined quantity

[5] https://www2.keck.hawaii.edu/inst/deimos/dsim.html

[6] For slit PAs other than 0° and 180°, movement along the major axis of the slit also results in movement to the east or west, the magnitude of which is governed by the PA of a given slit. However, once the ambiguity between the directionality of the slit array in the north/south directions is set, the components of the movement per spatial pixel in each of the cardinal directions becomes a trivial calculation.

[7] This is referred to as the "raw" value here as the spatial centroid will be corrected for differential atmospheric refraction later in this section.
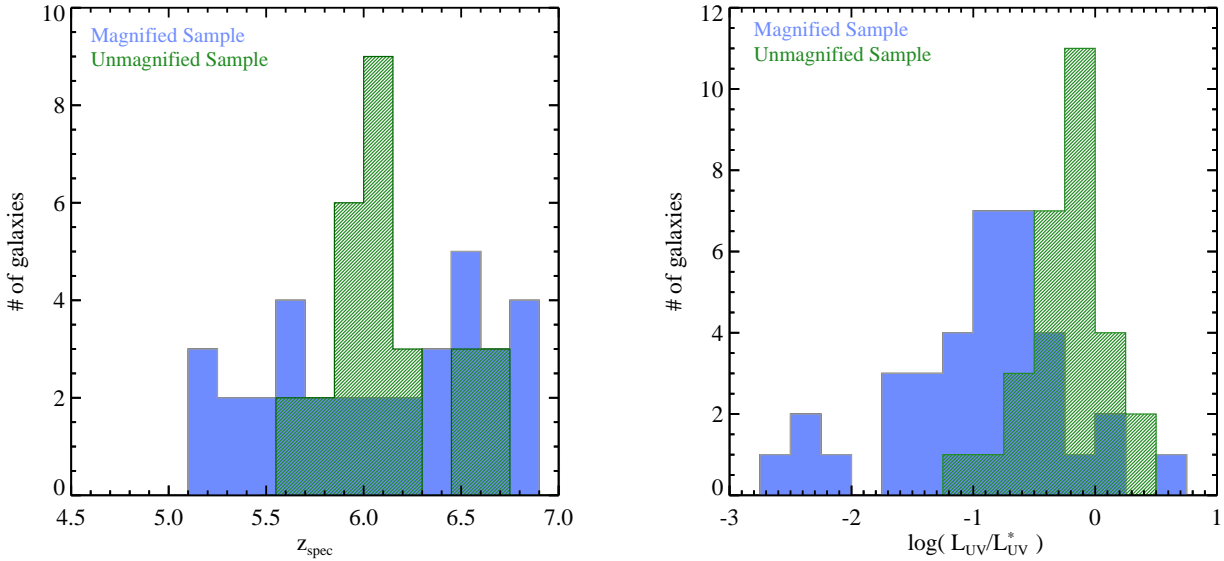
Figure 1. *Left*: Redshift distribution of our final lensed (blue solid histogram) and unlensed (green hatched histogram) sample of high-redshift Lyα emitters. The two samples are demarcated at $0.25 L_{UV}/L_{UV}^*$ in order to create sub-samples of roughly equal size. One lower-redshift galaxy at $z_{spec} = 4.4830$ taken from the sample of Fuller et al. (2020) is outside the bounds of this plot. *Right:* Estimate of the rest-frame UV luminosity (magnification corrected when applicable) relative to the characteristic UV luminosity at the redshift of each galaxy taken from Bouwens et al. (2015). The colors and shading are identical to the left panel. The median UV luminosity of the combined sample is $\log(\widetilde{L_{UV}}/L_{UV}^*) = -0.5$ and the entire sample spans approximately three and a half orders of magnitude in L_{UV}.

estimated μ values, as estimated from the interquartile range of bootstrap-resampled maps (see Hoag et al. 2019b for more details), are small enough to be ignorable for the vast majority of galaxies. Specifically, the median uncertainty resulting from this process is 3%, with < 5% of our sample showing magnification uncertainties >15%, a negligible uncertainty considering the $\sqrt{\mu}$ dependence of our results. For the latter, the variation in μ as derived by different modeling approaches, we performed the following test. For the ∼40% of our galaxies that lie within the HFFs, we calculated the 3σ clipped mean of the μ values for a large variety of models provided on a web-based tool specifically designed to compare the results of different models[8] and compared these to the μ values coming from our models. While individual estimates had sigma-clipped dispersions of factors of ∼2-3, the values of μ coming from our models were, on average, statistically consistent with the aggregate mean. Thus, while lensing-corrected $|\Delta_{Ly\alpha-UV}|$ values for individual galaxies likely contain an additional uncertainty factor of $\sqrt{2} - \sqrt{3}$ due to our ignorance of the true μ value, this uncertainty likely does not affect the average values that the main conclusions of this paper are based on.

2.2 Unmagnified Sample

The second sample of galaxies used in this work, which we will broadly refer to as the "unmagnified sample" as these observations are taken in legacy fields mostly devoid of massive, lower-redshift structure, was drawn from the samples of Pentericci et al. (2011) and Pentericci et al. (2018b), with a few additional galaxies taken from Caruana et al. (2014). These galaxies were observed with FOcal

---

[8] https://archive.stsci.edu/prepds/frontier/lensmodels/webtool

Reducer/low dispersion Spectrograph 2 (FORS2; Appenzeller et al. 1998) equipped on the Very Large Telescope (VLT) Antu Unit Telescope and selected for spectroscopy through a variety of dropout and color criteria. Except for a few galaxies contained in the New Technology Telescope Deep Field (NTTDF; Arnouts et al. 1999; Fontana et al. 2000) and the BDF-4 field (Lehnert & Bremer 2003; Castellano et al. 2010), all galaxies in this sample were observed with deep multi-band *HST*/ACS and WFC3 imaging as part of the Cosmic Assembly Near-infrared Deep Extragalactic Legacy Survey (CANDELS; Grogin et al. 2011; Koekemoer et al. 2011). In all cases, slit widths were set to 1″. For more details on the imaging and spectral observations of this sample, see Pentericci et al. (2018b) and references therein.

We also considered the inclusion of additional galaxies drawing from the $5 \leq z \leq 6$ presented in Khusanova et al. (2020) to supplement the unmagnified sample. This sample, which is comprised both of LAEs and non-emitters observed with extremely deep low-resolution spectra from the Visible Imaging Multi-Object Spectrograph (VIMOS; Le Fèvre et al. 2003) previously mounted on the VLT Melipal Unit Telescope, represents the high-redshift tail of galaxies in the VIMOS Ultra-Deep Survey (VUDS; Le Fèvre et al. 2015). However, despite the extremely deep spectroscopy, we were only able to reliably measure $|\Delta_{Ly\alpha-UV}|$ for a sub-sample of six LAEs due primarily to lack of observed continuum and uncertainty in the expected UV location of the target in the reduced data. While these six galaxies are included as a comparison to our data in §3.1, due to the relatively small number of galaxies and the differing selection, observational strategy, and methods used to measure associated quantities for these galaxies, we chose not to include these galaxies in our final sample. We note, however, that none of the results presented in this study are meaningfully changed if we instead included these galaxies as part of the unmagnified sample.

2.2.1 *Lyα and Rest-frame UV Spatial Centroids of the Unmagnified Sample*

For this sample, the continuum was observed for a large number of galaxies, and, as such, a more direct approach could be taken to measure the offset between Lyα and the continuum. For each of the ∼50 galaxies in the sample, the Lyα location was measured using the methods given in section 2.1.1 with the Gaussian method always preferred except in low-S/N cases. In the absence of formal error spectra, errors were assumed to be Poissonian. Though such an assumption likely underestimates the true noise, the results did not meaningfully change if we instead scale the errors to match the average root-mean-square fluctuations. To measure the UV centroid, the flux over the same spatial window was summed over a broad spectral window at least 10Å in the observed-frame redward of the observed Lyα line. The spectral window employed changed based on the target to avoid regions of dominant skylines and those regions where the continuum signal was minimal, but was typically several 100Å (observed-frame) wide. The reduction process of the FORS2 data employed spatial trimming of the data in order to maximize the effectiveness of the sky subtraction. At the completion of this process, the information on the expected location of the galaxies was no longer encoded in the data, and, as such, only galaxies with well-measured continuum and Lyα centroids were allowed to remain in our sample. This cut resulted in a total of 29 galaxies. The $|\Delta_{\mathrm{Ly}\alpha-\mathrm{UV}}|$ was then calculated in a similar manner to those in magnified sample using the appropriate plate scale, though, since Lyα and continuum centroids were measured at similar wavelengths, no DAR correction was applied to either value. Additionally, since galaxies in this sample are, at least to first approximation, not lensed modulo small weak-lensing effects that may occur along a random line of sight, no lensing correction to the measured offset is applied. The median redshift of the 29 galaxies in this sample is $\tilde{z}_{spec}$=6.05 and the redshift distribution is shown in the left panel of Figure 1.

Because we are using different approaches to estimate $|\Delta_{\mathrm{Ly}\alpha-\mathrm{UV}}|$ in the lensed and unlensed sample, we compared the $|\Delta_{\mathrm{Ly}\alpha-\mathrm{UV}}|$ distribution for the two samples where there was overlap in intrinsic UV luminosity. No statistically significant difference was found from a Kolmogorov-Smirnov (K-S) test. Additionally, a Spearman's test finds no evidence of significant correlation between $|\Delta_{\mathrm{Ly}\alpha-\mathrm{UV}}|$ and the S/N of either the Lyα detection or the UV continuum in the spectroscopy (the latter could be tested only in the case of the unlensed sample). These tests indicate that any observed Lyα-UV offset is likely to be real and not the result of poor centroiding.

2.3 Associated Quantities

In §3.1 we will explore whether $|\Delta_{\mathrm{Ly}\alpha-\mathrm{UV}}|$ depends on several basic properties of the galaxies as estimated through the various spectroscopic and imaging observations. These properties are the spectral redshift, the intrinsic (i.e., lensing corrected) far-UV luminosity relative to the characteristic equivalent luminosity at the redshift of the galaxy (L_{UV}/L_{UV}^*), the intrinsic Lyα line luminosity ($L_{\mathrm{Ly}\alpha}$), and the rest-frame equivalent width of the Lyα line ($EW_{\mathrm{Ly}\alpha}$). We quickly review how these quantities were estimated for our data.

For the magnified sample, L_{UV} is estimated using the apparent magnitude of each LAE in the $F160W$ band, with a $k-$correction applied to convert to rest-frame ∼1600Å, and we convert to an intrinsic value by dividing the k-corrected L_{UV} by the most likely magnification value, μ. The redshift-dependent characteristic UV luminosity, L_{UV}^*, is taken from Bouwens et al. (2015). The $L_{\mathrm{Ly}\alpha}$

for each galaxy is estimated from the observed line flux corrected for slitloss effects assuming that the UV location and the Lyα line are co-located with respect to the slit. These values are also corrected for the magnification. The $EW_{\mathrm{Ly}\alpha}$ values are calculated using the de-magnified line luminosity and the rest-frame UV flux density was estimated from a filter whose throughput begins just redward of the observed wavelength of Lyα (typically $F105W$). For more details on these calculations see Fuller et al. (2020).

For the unmagnified sample, equivalent values were drawn directly from the relevant references when available. In the case of Pentericci et al. (2011, 2018b), rest-frame absolute magnitudes (M_{UV}) were calculated in a similar manner to those in our magnified sample and were subsequently converted to L_{UV}/L_{UV}^* values again using the L_{UV}^* of Bouwens et al. (2015). In those works, slit losses were assumed to be small (∼15%) and were not included in estimating Lyα line luminosities and EWs. The $EW_{\mathrm{Ly}\alpha}$ values reported in those papers also relied on flux density measured in the broadband photometry in order to quantify the strength of the continuum redward of Lya. Additional data from the literature had their equivalent quantities derived in a similar manner. For more details, see Pentericci et al. (2018b). In the right panel of Figure 1 we show the L_{UV}/L_{UV}^* distribution for both the magnified and unmagnified sample.

2.4 Rest-frame UV Morphology and Galaxy Sizes

For all galaxies in both samples, save those few galaxies in the NTTDF and BDF-4 fields for which such imaging was not available, we visually inspected a HST/WFC3 $F160W$ postage stamp. This inspection was done to look for multiple clumps or other obvious features that may suggest that any appreciable Lyα-UV offset is caused by merging activity or issues with centroiding the emitting galaxy in the UV. The observed $F160W$ band corresponds to rest-frame ∼2250Å for the median redshift of the combined sample ($\tilde{z}_{spec}$ = 6.15). In the majority of cases (∼65%), the galaxy was observed to be an isolated galaxy with a reasonably symmetric surface brightness profile. The remaining ∼35% appeared to be multicomponent systems, but the vast majority had either a slit orientation that was nearly perpendicular to the position angle of the multiple clumps that comprised the galaxy (see, e.g., the left panel of Figure 2) or the directionality of the measured Lyα-UV offset was opposite that of the direction to the secondary clump(s)[9]. We therefore conclude that the $|\Delta_{\mathrm{Ly}\alpha-\mathrm{UV}}|$ values measured in our sample are primarily the result of true *intra*galaxy astrophysical offsets and do not result from misidentification of the original source or bad UV centroiding due to multiple components.

In addition to qualitatively characterizing the morphology and multiplicity of our LAE samples, we also measured effective radii (r_e) using a combination of SOURCE EXTRACTOR (SEXTRACTOR; Bertin & Arnouts 1996) and PSFEX (Bertin 2011) to perform point-spread function (PSF)-corrected Sérsic fits on all galaxies imaged in HST/WFC3 $F160W$. We chose to focus only on those galaxies with HST imaging, which included all galaxies in the magnified and sample and 24 galaxies in the unmagnified sample, with the Sérsic index treated as a free parameter. Extremely low S/N or visual reduction artifacts in the $F160W$ imaging caused the loss of ∼30% of

---

[9] Images for the magnified sample and the vast majority of the unmagnified sample are publicly available and slit orientations are shown in Pentericci et al. (2018b); Fuller et al. (2020) (for the former, slit PAs are identical those of the masks).
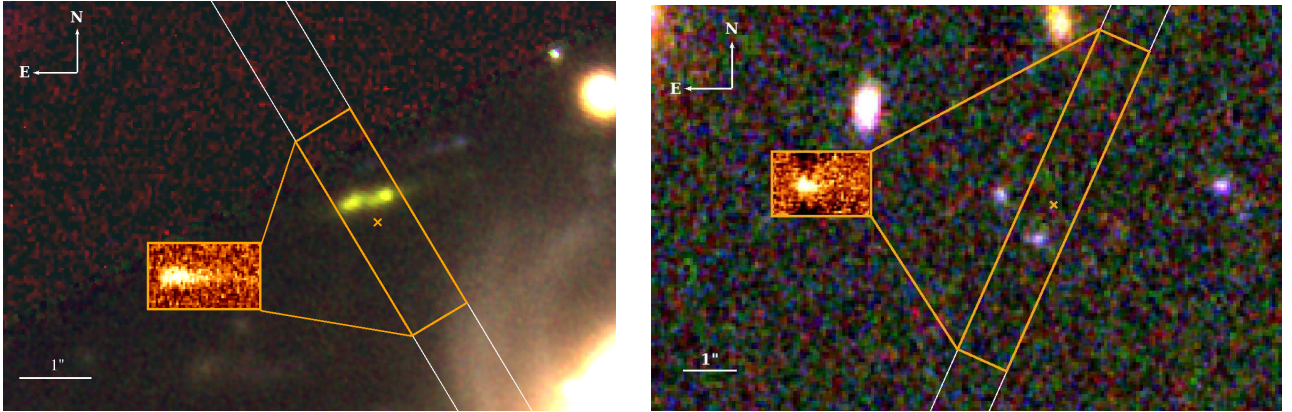
Figure 2. *Left:* Example of a magnified galaxy (ID=370.14 in Fuller et al. 2020) with an offset of $|\Delta_{Ly\alpha-UV}| = 0.67$ kpc after correcting for lensing effects ($\mu = 8.94$). This offset is typical for our full sample of LAEs, though on the large end for a lower-luminosity galaxy ($L_{UV}/L_{UV}^* = 0.22$). The background image is a $F814W/F105W/F160W$ color composite. The slit used to observe this galaxy is outlined in white. A portion of the two-dimensional spectrum corresponding to the spatial region highlighted in orange and the spectral region of the Lyα line is shown in the inset. Note that the two-dimensional spectrum inset is rotated and rectified for clarity such that the spatial axis, i.e., the direction along the major axis of the slit, is vertical. The observed spatial centroid of the Lyα line is shown as the orange ×. Note that while this galaxy exhibits multiple components possibly indicative of a companion or multiple star-forming clumps, the direction of the Lyα offset is perpendicular to the position angle of these components. For reference, a scale bar indicating $1''$ is shown in the bottom left. *Right:* Similar to the left panel, but for the unmagnified galaxy UDS-23719 taken from Pentericci et al. (2018b). An $F125W$ image is used in the green channel as a substitute to $F105W$. This galaxy exhibits the largest offset in the full sample, with $|\Delta_{Ly\alpha-UV}| = 3.65$ kpc.

the galaxies in the magnified sample and one additional galaxy in the unmagnified sample. As in §2.1.2, for magnified galaxies, measured r_e were corrected to intrinsic by dividing by $\sqrt{\mu}$. Galaxies with multiple components were measured using SEXTRACTOR parameters specifically tuned to blend the multiple components and perform the Sérsic fit on the composite system. This process resulted in a final sample of 48 galaxies with reliable r_e measurements with an average $\tilde{r}_e = 0.6$ kpc, consistent with parametric measurements of other galaxy samples at similar redshifts (see, e.g., Shibuya et al. 2015, 2019; Curtis-Lake et al. 2016; Paulino-Afonso et al. 2018). In later sections, we will compare these UV sizes with their respective Lyα-UV offsets. All UV sizes, Lyα-UV offsets, and all other properties of galaxies in the unmagnified and magnified samples are given in Tables 1 and 2, respectively.

3 RESULTS

3.1 Size and Pervasiveness of Lyα-UV Offsets

The filled gray histogram in the left panel of Figure 3 shows the combined distribution of $|\Delta_{Ly\alpha-UV}|$ for the lensed and unlensed sample. The median value of the offset for the full sample, 0.61 kpc, is given in the top right of Figure 3, along with the effective 1σ normalized median absolute deviation (NMAD; Hoaglin et al. 1983) scatter on the offset (0.68 kpc). The typical uncertainty on $|\Delta_{Ly\alpha-UV}|$ for the entire sample is 0.30 kpc, where uncertainties are derived only from the measurement process and do not include uncertainties associated with lensing or DAR corrections. While two-thirds of the entire sample have offsets significant at the $\geq 1\sigma$ level and ~40% at the $\geq 3\sigma$ level, at a cursory level, these offsets appear to be generally small. However, >10% of our sample appear with Lyα-UV offsets that exceed 2 kpc and the largest offsets reach up to nearly 4 kpc, offsets that exceed the half-width of our DEIMOS slits and would have a considerable detrimental effect on our ability to detect these galaxies in Lyα if this offset had been perpendicular to the spatial axis of our slits (see §3.4). Additionally, as mentioned earlier, due to projection effects, such measurements represent *lower*

limits to the true physical separation between the peak of the Lyα and UV continuum emission. We note here, however, that it is unlikely that our observations missed even larger offsets, at least those that are somewhat aligned with the major axis of our slits, as most galaxies were observed with slits designed to have ~10-20 kpc of space on either side of the galaxy even after accounting for lensing effects.

From Spearman correlation coefficient tests, we find no evidence of significant correlation between $|\Delta_{Ly\alpha-UV}|$ and either the $EW_{Ly\alpha}$ or the Lyα line luminosity. The lack of both is perhaps surprising since larger offsets should generally depreciate the measured line luminosity, or, equivalently, the EW at fixed UV luminosity, if they occur isotropically. However, it is possible that we are only able to detect offsets in those galaxies for which the offsets are primarily parallel to the major axis of the observed slits. Additionally, we do not have the ability to control for the intrinsic line luminosity, which further confuses this comparison. As such, we do not discuss this lack of correlation further opting instead to quantify slit losses for a variety of different spatial offsets in §3.4.

Additionally, we see no evidence within our own sample of evolution in $|\Delta_{Ly\alpha-UV}|$ as a function of redshift. A Spearman test returns no significant rejection of the null hypothesis that the two variables are uncorrelated, nor does a K-S test when breaking the sample into a lower and higher redshift sample. As can be seen in the right panel of Figure 3, both small and large offsets are seen at essentially all redshifts probed by the combined sample.

In Hoag et al. (2019a), based on a sample of ~300 LAEs in the redshift range $3 \leq z \leq 5.5$ taken from the VANDELS survey (McLure et al. 2018; Pentericci et al. 2018a), it was suggested that both the apparent and physical offsets between UV continuum and Lyα emission may decrease with increasing redshift. However, limitations in the statistical significance of the result occurred at the high-redshift end of the VANDELS sample ($z \geq 4.5$). Here, we compare our projected offset distribution with the equivalent quantity measured in Hoag et al. (2019a) (see Figure 2 of Hoag et al. 2019a) using identical redshift binning. We find no significant evidence of a difference between the distribution of projected offsets
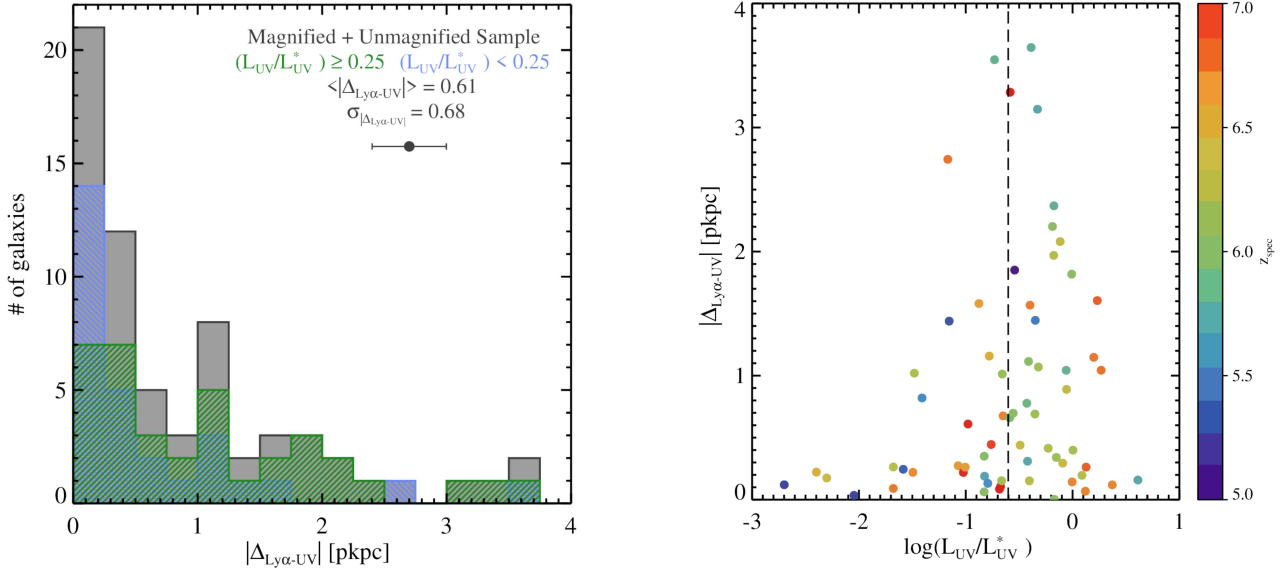
Figure 3. *Left:* Distribution of the Lyα and UV continuum spatial offset for our full (gray solid), fainter (light blue hatched), and brighter (green hatched) samples. The definition of the two luminosity samples along with the median offset and NMAD scatter of the full sample is given in the top right. The average measurement uncertainty for the combined sample is also shown. *Right:* Lyα-UV spatial offset plotted against L_{UV}/L_{UV}^* for our full sample. The color bar indicates the spectroscopic redshift of each galaxy. The dashed line shows the delineation point between our lower- and higher-luminosity samples. There is a marginally significant positive correlation observed between $|\Delta_{Ly\alpha-UV}|$ and L_{UV}/L_{UV}^*, and the UV-brighter sample shows both a larger percentage of significant offsets and a larger median offset than their lower-luminosity counterparts (0.89±0.18 vs. 0.27±0.05 kpc, respectively). As discussed in §3.1, this difference is likely not due to observational effects and rather represents real differences between the two galaxy populations. No significant correlation is observed as a function of redshift within this sample.

in our sample at $z \sim 6$ and the full sample of Hoag et al. (2019a). Additionally, we do not find any significant differences between the two samples if we match the samples by UV luminosity or combine the two samples and bin by redshift.

An identical comparison was also made to ~900 LAEs observed at $2 \le z \le 6$ ($\bar{z} = 2.9$) as part of the VUDS survey[10]. For this subset of VUDS LAEs, Ribeiro et al. (2020) present spatial offset measurements made on the observed continuum and the Lyα feature. In an internal comparison of these ~900 LAEs, marginal evidence was found of redshift evolution in the projected one-dimensional spatial offsets, with increasing redshifts leading to slightly smaller offsets. Comparing the median projected offset found for the sample in Ribeiro et al. (2020) (0.60±0.05 kpc) to those found in our sample, 0.61±0.08 kpc, suggests no significant redshift evolution. This lack of significant difference persists when performing a K-S test on the two distributions, compare to subsamples in different redshift bins, or (UV) luminosity match the data. We additionally compare both of these samples and our own sample to the spatial offsets of the six galaxies at $5 \le z \le 6$ from Khusanova et al. (2020) for which we could reliably measure an offset (see §2.2). The median offset for this sample, 0.51±0.12 kpc, is statistically consistent with those of all other samples. Median spatial offsets of various redshift and luminosity sub-samples drawn from these four samples are plotted in Figure 4. With a large sample

available at all redshifts from $2 \le z \le 7$, the lack of significant difference in the offset distributions implies that whatever processes govern the offset of Lyα emission from the UV continuum are, at least, not a strong function of redshift.

It does appear, however, within our own sample that the processes governing Lyα offsets are related to the UV luminosity of the host galaxy. In the right panel of Figure 3 offsets are plotted as a function of L_{UV}/L_{UV}^* and in the left panel the offset distribution is shown for galaxies that are brighter and fainter than $0.25L_{UV}^*$, which is roughly $M_{UV} \sim -19.5$. This splitting resulted in 36 galaxies in the brighter sample and 29 galaxies in the fainter sample. Note that the choice of this luminosity was made to create roughly equal-sized samples and none of our results change meaningfully if we delineate at a UV luminosity that is up to ~50% brighter or fainter than the fiducial luminosity. Offsets generally appear to increase with increasing (UV) brightness, with a Spearman test returning evidence for a positive correlation ($\rho_{Spearman} = 0.21$) at a ~2σ level and a K-S test returning a rejection of the null hypothesis that the two distributions are drawn from a common underlying sample at the ~3σ level. Note that these statements are not particularly sensitive to the exact ranges chosen to define the two samples, as the Spearman test is independent of this choice, and a K-S test rejects the null hypothesis at the $\gtrsim 2\sigma$ level irrespective of the exact choice of L_{UV}/L_{UV}^* used to delineate between the faint and bright samples. While offsets for galaxies of all UV luminosities generally tend to be small, the vast majority (~ 80%) of the larger offsets (≥ 1.5 kpc) are observed in the brighter sample. Further, the median offset for the brighter sample, 0.89±0.18 kpc, is approximately three times larger than that of the fainter sample, 0.27±0.05 kpc. Though the dependency of $|\Delta_{Ly\alpha-UV}|$ on UV luminosity varies with the

[10] Note that this sample largely does not include those galaxies presented in Khusanova et al. (2020) which, for completeness, were combined with our final sample and used as a high-redshift point of comparison for this exercise in addition to a comparison solely to our final sample.

Table 1. Properties of the Unmagnified LAEs

ID	RA	Dec	z_{spec}	$|\Delta_{Ly\alpha-UV}|$ [pkpc]	r_e [pkpc]	L_{UV}/L_{UV}^*	$\log(L_{Ly\alpha})$ [ergs s^{-1}]	$EW(Ly\alpha)_{rest}$ [Å]
GOODS-10219	53.2020264	-27.816353	6.136	2.0±0.4	1.2±0.6	0.67	42.3	14
GOODS-11464	53.1174545	-27.805187	5.939	2.2±0.4	0.5±0.2	0.65	42.5	22
GOODS-14439	53.1248894	-27.784107	5.783	0.8±0.2	1.6±0.1	0.37	42.6	50
GOODS-15443	53.1519432	-27.778177	5.938	1.8±0.7	$0.9^{+2.5}_{-0.9}$	0.98	42.2	7
GOODS-16371	53.1595078	-27.771446	6.108	0.4±0.7	0.6±0.5	0.59	42.1	11
GOODS-17692	53.1627693	-27.760759	5.916	0.1±0.4	0.3±1.2	0.15	43.0	153
GOODS-17720	53.1225586	-27.760504	5.927	1.1±0.9	1.0±0.7	0.39	42.4	30
GOODS-18310	53.1419334	-27.755154	6.046	0.2±0.5	0.5±0.2	0.22	42.1	26
GOODS-31891	53.1742516	-27.769789	6.630	2.7±0.7	—^{a}	0.07	42.0	73
GOODS-32453	53.1799088	-27.754873	5.929	0.7±0.3	$0.6^{+1.4}_{-0.6}$	0.28	42.5	56
GOODS-33418	53.1944962	-27.726349	7.058	3.3±0.3	0.2±0.2	0.26	42.9	110
UDS-1920	34.4887581	-5.2656999	6.565	0.1±0.3	0.9±0.4	2.35	42.2	3
UDS-4812	34.4757347	-5.2484999	6.561	0.3±0.1	$0.5^{+0.6}_{-0.5}$	0.99	43.0	44
UDS-4872	34.4820328	-5.2481742	6.564	0.1±0.3	0.7±0.3	1.32	42.4	10
UDS-14549	34.4828377	-5.1953101	6.033	0.7±0.3	$0.3^{+0.4}_{-0.3}$	0.44	42.3	20
UDS-15559	34.2315788	-5.1897931	6.044	0.4±0.2	$0.4^{+0.7}_{-0.4}$	1.01	42.5	79
UDS-18087	34.3972206	-5.1756892	6.119	0.2±0.2	$0.4^{+0.5}_{-0.4}$	1.22	43.2	47
UDS-23719	34.3104324	-5.1456208	5.683	3.6± 0.2	$0.7^{+1.4}_{-0.7}$	0.41	42.6	64
UDS-28306	34.3560867	-5.2582278	6.142	0.2±0.1	1.1±0.7	0.39	42.5	41
UDS-29191	34.5253906	-5.2412128	5.943	0.0±0.3	$0.3^{+0.5}_{-0.3}$	0.67	42.6	34
COSMOS-7692	150.107757	2.2719180	6.046	0.1± 0.1	1.9±0.2	0.48	42.5	24
COSMOS-21411	150.183018	2.4392050	6.221	0.3±0.3	1.0±0.6	0.81	43.2	90
COSMOS-24108	150.197222	2.4786510	6.629	1.0±0.3	1.6±1.3	1.85	43.0	27
NTT-6345	181.403901	-7.7561900	6.701	1.6±0.3	—^{a}	1.70	41.7	15
NTT-7246	181.380139	-7.7700590	5.724	1.0±0.4	—^{a}	0.87	42.2	12
BDF-3995	336.979035	-35.179460	6.198	2.1±0.6	—^{a}	0.77	42.0	7
BDF-4085	336.957328	-35.181049	6.196	0.9±0.2	—^{a}	0.88	43.0	110
BDF-5870	336.955504	-35.208964	5.632	3.1±0.3	—^{a}	0.47	41.8	10

^{a} No *HST*/WFC3 *F*160*W* imaging or insufficient S/N

comparison being made and the exact sample definition, the positive correlation between the two ranges from marginally to highly significant across all combinations and always favors larger offsets in UV-brighter galaxies. This relationship also appears to persist at approximately the same level of significance when estimating the instrinic offset distributions for the two luminosity sub-samples (see §3.2 and Appendix B).

These results remain broadly unchanged if we excise the most highly-magnified galaxies from our sample ($\mu > 50$). These are the galaxies in our sample where the lensing approximation given in §2.1.2 is likely to have the largest effect. However, even after excising the highly-magnified galaxies, it is still possible that the difference we observe here could be attributed, at least in part, to small-scale lensing effects rather than any true physical differences between the samples. This would be the case only if this lensing approximation is not valid *on average* for the ~ 25 remaining magnified galaxies. Unfortunately, the equivalent exercise of comparing offsets to comparably UV-fainter galaxies as our lower-luminosity sample cannot be performed on the data in Hoag et al. (2019a) or Ribeiro et al. (2020), as both studies only probe galaxies with UV

luminosities that are comparable to our brighter sample. Larger samples at lower-luminosity as well as better modeling of local lensing effects will be necessary to disambiguate the possible origins of this difference.

In a standard flux-limited survey in a blank field, in order to make a robust claim about differences observed as a function of galaxy brightness, it is necessary to mitigate issues related to Malmquist bias and differential selection effects relating to the difference in the intrinsic brightness of the sources of interest. In a spectroscopic survey employing slit observations, it would additionally be necessary to discuss any differential loss of light between the two populations as a resulting from the peculiarities of spectroscopic observations with finite-width slits. In the measurements presented here, this may be seen as particularly important, as it may be that we are simply missing the large-offset tail of lower-luminosity galaxies due to excess slit loss on a population that would, in a typical flux-limited field survey, be near the edge of detectability.

However, one of the many virtues of a survey of lensed candidates is that the relationship between intrinsic brightness and the expected flux is modulated. Additionally, we are binning galaxies by

Table 2. Properties of the Magnified LAEs

| ID	RA	Dec	z_{spec}	$\|\Delta_{Ly\alpha-UV}\|^a$ [pkpc]	r_e^a [pkpc]	$L_{UV}/L_{UV}^{*\,a}$	$\log(L_{Ly\alpha})^a$ [ergs s^{-1}]	$EW(Ly\alpha)_{rest}$ [Å]	μ_{med}
2744.116	3.592285	-30.409911	6.101	1.0±2.0	$1.5^{+2.1}_{-1.5}$	0.03	41.5	223	4.3
370.14	39.978069	-1.558956	6.572	0.7±0.1	0.8±0.4	0.22	42.0	80	8.9
370.43	39.966302	-1.587095	6.612	0.1±1.2	1.3±0.2	0.02	40.8	97	8.4
370.55	39.990193	-1.571209	5.614	0.2±0.1	0.3±0.3	0.15	41.9	101	3.2
0416.17	64.036510	-24.092300	5.993	1.0±0.2	$—^b$	0.22	41.9	66	2.6
0416.56	64.047848	-24.062069	6.146	0.3±0.3	0.3±0.1	0.02	40.8	105	22.6
0416.89	64.048668	-24.082184	5.241	1.4±0.3	0.2±0.3	0.07	41.2	35	2.2
0717.15	109.3923348	37.738083	5.470	0.1±0.1	$—^b$	0.16	41.0	17	37.9
0717.17	109.3914431	37.767048	5.458	0.8±0.4	$1.0^{+2.6}_{-1.0}$	0.04	41.4	69	4.0
0717.25	109.4077276	37.742741	6.374	1.2±0.1	$—^b$	0.17	42.4	145	2.7
0717.53	109.4128542	37.733804	6.348	0.2±0.1	0.23±0.01	0.004	40.7	17	34.8
0717.59	109.37792	37.742851	5.637	0.2±0.4	3.7±0.1	4.09	41.2	1	2.0
0744.17	116.202128	39.44821	5.718	3.5±0.7	$—^b$	0.19	41.2	26	1.2
0744.60	116.22109	39.441155	5.899	0.4±0.2	$0.2^{+0.3}_{-0.2}$	0.15	41.6	57	3.8
1149.51	177.413006	22.418862	6.694	0.3±0.5	0.6±0.2	1.34	41.7	17	1.8
1149.67	177.412021	22.415777	6.621	1.1±0.3	1.3±0.1	1.57	41.7	6	1.8
1347.4	206.895685	-11.754647	6.598	1.6±0.7	1.6±0.8	0.4	41.9	76	1.4
1347.25	206.8706306	-11.753105	6.254	0.2±0.5	0.1±0.1	0.005	39.5	25	177.1
1347.28	206.8750764	-11.7588426	6.544	0.2±0.4	0.16 ±0.01	0.03	40.9	58	15.6
1347.29	206.8865703	-11.7620709	5.194	0.1±0.9	0.12±0.02	0.002	39.4	33	143.9
1347.36	206.903015	-11.750369	6.471	0.3±0.1	$0.2^{+0.4}_{-0.2}$	0.09	41.8	112	4.1
1347.39	206.8886406	-11.754282	5.286	0.2±0.5	0.4±0.2	0.03	40.0	9	21.2
1347.45	206.8816569	-11.761483	5.194	0.0±1.4	$—^b$	0.01	39.4	17	77.7
1347.47	206.900859	-11.754209	6.771	0.4±0.2	0.01±0.01	0.17	41.7	55	5.2
1423.13	215.928816	24.083906	5.699	2.4±0.4	1.6±0.6	0.67	41.2	13	1.7
1423.16	215.928929	24.072848	7.101	0.1±0.1	$—^b$	0.21	42.6	189	1.4
1423.17	215.972591	24.072661	6.450	1.6±0.2	1.6±0.5	0.13	42.0	125	1.4
1423.26	215.935869	24.078415	6.226	0.4±0.1	0.96±0.03	0.32	41.6	59	2.1
1423.37	215.93618	24.074682	4.483	1.9±0.2	1.2±0.5	0.29	40.0	4	2.1
1423.38	215.93638	24.057093	5.389	1.4±0.1	$—^b$	0.45	41.9	42	1.9
2129.5	322.36419	-7.701938	6.458	0.3±0.3	$—^b$	0.10	41.7	116	2.7
2129.22	322.350939	-7.693331	6.846	0.1±0.2	$—^b$	0.21	42.1	100	3.8
2129.28	322.336347	-7.696575	5.628	0.3±0.3	$—^b$	0.38	41.9	37	1.9
2129.31	322.353238	-7.697444	6.846	0.2±0.1	0.2±0.2	0.10	41.6	58	5.4
2129.36	322.353941	-7.681644	6.846	0.6±0.2	$—^b$	0.11	42.1	82	1.2
2214.1	333.7234552	-14.014297	5.847	0.7±0.1	1.2±1.2	0.15	42.4	407	1.5

^{a} Corrected for best-fit magnification ^{b} No *HST*/WFC3 *F*160*W* imaging, insufficient S/N, or reduction artifact

their intrinsic UV luminosity, whereas we are discussing the measurement of the Lyα line, a relationship which is further modulated by complicated processes internal to the emitting galaxies. In our own sample, while there is a strong and significant positive correlation between the magnification-corrected Lyα line luminosity and intrinsic L_{UV}/L_{UV}^* ($\rho_{Spearman} = 0.59$, $p = 2e - 7$), there is, conversely, a strong and significant *anti*-correlation between the observed Lyα line flux and intrinsic L_{UV}/L_{UV}^* ($\rho_{Spearman} = -0.64$, $p = 9e - 9$). While large magnification values, values which would preferentially apply to the lower-luminosity sample, may re-

sult in pushing the Lyα emitting region out of the slit along the major axis in the case of relatively short slits, the typical (median) slit length of our observations is 10.3″ with an NMAD scatter of 3.3″. For galaxies near the center of the slit along the major axis, as, indeed, most targeted objects[11] are, as mentioned earlier, such

---

[11] Though this is not true for serendipitous detections, there are only three such galaxies in the lower-luminosity sample (∼ 10% of the sample), and the few that are in our sample are also reasonably well situated in the center of the major axis of the slit (Fuller et al. 2020)
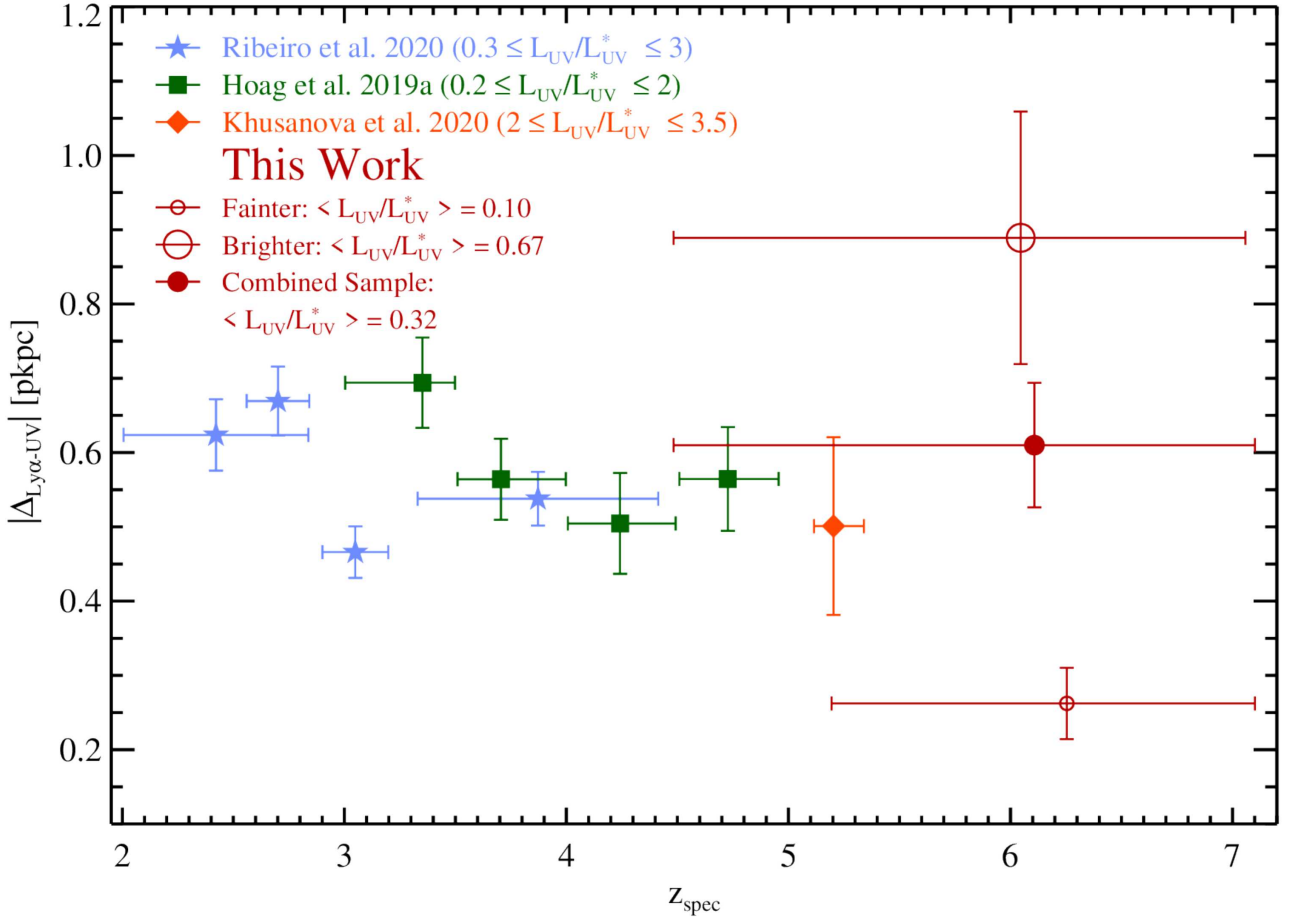
Figure 4. Plot of the median *projected one-dimensional* Lyα-UV spatial offset as a function of median redshift for a compilation of all survey measurements from $2 \le z \le 7$. The light blue stars show four equally-sized sub-samples at different redshift taken from Ribeiro et al. (2020), the green squares show four sub-samples at different redshift taken from the one-dimensional measurements from Hoag et al. 2019a, and the orange diamond shows the median value from our own measurement of six galaxies from the sample of Khusanova et al. 2020. The UV luminosity ranges of each sample are given in the legend at the top left. The red filled circle shows the median offset measured in our sample, with the large and small open red circles indicated those values for our brighter ($\ge 0.25 L_{UV}/L_{UV}^*$) and fainter ($< 0.25 L_{UV}/L_{UV}^*$) sub-samples. The median luminosities of our various (sub-)samples are given in the top left. In all cases, offset measurements represent lower limits to the true offsets in these galaxies. Vertical error bars indicate the error on the median estimated by the NMAD/$\sqrt{n-1}$, where n is the sample size (see Müller 2000; Lemaux et al. 2018). The horizontal error bars indicate the redshift extent of each (sub-)sample. No significant difference is found between the offset distributions or their medians for any of the samples at comparable luminosities. A significant difference is observed, however, between the median offsets of our fainter and brighter samples.

a length allows for ~10 kpc of space along the major axis at the median magnification of our lensed sample $\tilde{\mu} \sim 3$. Thus, it is unlikely that differential observational issues are responsible for the lower $|\Delta_{Ly\alpha-UV}|$ values observed in the lower-luminosity sample. We also note here that slit position angles for the magnified sample were not purposely oriented to along the magnified major axis of the galaxy, which would potentially differentially suppress or enhance our ability to detect offset Lyα for this sample relative to the unmagnified sample.

In §2.4 we measured the effective radii, r_e for the 48 galaxies in our full sample with sufficiently deep *HST*/*F*160*W* imaging to make a reliable measurement of this quantity. These 48 galaxies are comprised of 19 galaxies in the lower-luminosity sample and 29 in the higher-luminosity sample. Comparing $|\Delta_{Ly\alpha-UV}|$ to the

measured r_e values for the full sample, we find a reasonably strong and significant positive correlation ($\rho_{Spearman} = 0.35$, $p = 0.014$) between the two quantities, which implies that larger offsets originate from galaxies with larger UV extents. This difference is also reflected in the average (median) r_e of the two luminosity sub-samples, $\tilde{r_e} = 0.32 \pm 0.06$ and $\tilde{r_e} = 0.95 \pm 0.11$ for the lower- and higher-luminosity sub-samples, respectively, a trend consistent with results on photometrically-selected candidates at similar redshift in the HFFs (Kawamata et al. 2018). Interestingly, these two values are consistent with the average $|\Delta_{Ly\alpha-UV}|$ observed for each sample and the ratio between the two is essentially identical to that of the $|\Delta_{Ly\alpha-UV}|$ values in the two samples. We will come back to this concordance in §3.3.

3.2   An Estimate of the One-Dimensional Intrinsic Lyα-UV Offset Distribution

In the previous section we discussed the distribution of projected one-dimensional offsets as measured. However, as discussed extensively in Hoag et al. (2019a), the measured distribution differs from the intrinsic, though still one-dimensional and projected, distribution by the errors induced by the measurement process as well as any additional errors induced from the observations or analysis methods. In this section, we attempt to recover the intrinsic distribution of the offsets[12] by decoupling the spread induced through various errors from the intrinsic distribution.

We attempt two methods to decouple the errors from the measured distribution. Both methodologies model the observed distribution as the convolution of two Gaussians one resulting from observational, analysis, and measurement error, given by:

$$\Delta_{\text{Ly}\alpha-\text{UV, err}} = \frac{A'}{\sqrt{2\pi}\sigma_{err}} e^{\frac{-(\Delta-\mu_{err})^2}{2\sigma_{err}^2}} \quad (1)$$

where A' is the normalization, μ_{err} is the average offset, and σ_{err} is the spread in the distribution induced by observational, measurement, and analysis errors. The second Gaussian results from the instrinsic Lyα-UV offsets and is given by:

$$\Delta_{\text{Ly}\alpha-\text{UV, int}} = \frac{A''}{\sqrt{2\pi}\sigma_{int}} e^{\frac{-(\Delta-\mu_{int})^2}{2\sigma_{int}^2}} \quad (2)$$

where μ_{int} and σ_{int} are the average intrinsic offset and the intrinsic spread of the distribution, respectively. The measured distribution is then:

$$\Delta_{\text{Ly}\alpha-\text{UV, err}} \otimes \Delta_{\text{Ly}\alpha-\text{UV, int}} =$$
$$\frac{A}{\sqrt{2\pi}\sqrt{\sigma_{err}^2 + \sigma_{int}^2}} e^{\frac{-(\Delta-\mu)^2}{2(\sigma_{err}^2+\sigma_{int}^2)}} \quad (3)$$

where $\mu \equiv \mu_{err} + \mu_{int}$ (though see the note on μ_{int} later in this section).

In this section we describe the first of the two methods, in which fits are performed to the observed distributions and the intrinsic distributions are inferred from those fits. A second method, in which we calculate the likelihood distribution of σ_{int} is presented in Appendix B. The method described in Appendix B returns statistically consistent results to the method described in this section.

For this first method, rather than simply fit the expression in Equation 3 to the observed distribution of the various samples, we instead opted for a Monte Carlo process in which we tweaked each offset measurement by Gaussian sampling its formal random uncertainties 1000 times and a fit is performed on each realization. For each fit, the larger of the two σ values was adopted as that due to astrophysically-induced offsets (i.e., σ_{int}). This is likely a reasonable assumption, as the measured offsets are generally larger than our estimated errors. Additionally, as we will show later, the recovered σ_{err} distribution is consistent with our average estimated error. Under the assumption that our errors are Gaussian and that

we have accurately accounted for all sources of uncertainty, such a methodology allows us to create a probability density function (PDF) of the intrinsic distribution. From the resulting PDFs, we adopt the median and the 16th/84th percentiles as the values of σ_{err} and σ_{int} and their associated uncertainties, respectively. As an added benefit to this process, we can check whether there are hidden sources of observational or measurement error by examining the PDF of σ_{err}. If the median value of σ_{err} differs appreciably from our median formal error (0.25-0.30 kpc depending on the sample) or its uncertainties are inconsistent with σ_{err} being zero, as some Monte Carlo realizations are likely to stumble on the true distribution, then it is likely there are unaccounted sources of error.

In Figure 5 we plot the observed distribution of $|\Delta_{\text{Ly}\alpha-\text{UV}}|$ for the higher-luminosity, lower-luminosity, and full with accompanying error bars reflecting the variation in the bin numbers across all 1000 Monte Carlo realizations. Overplotted on these observed distributions is the median fit to all Monte Carlo realizations along with a shaded region representing the 1σ region, i.e., the 16th/84th percentiles of each fit distribution. In each panel we indicate the median values of σ_{err} and σ_{int} and their associated uncertainties, as well as the median χ_ν^2 for the 1000 realizations. Note that, in each case, the mean of the convolved Gaussian given by μ in Equation 3 was statistically consistent with zero. Such a result is encouraging as, modulo statistical fluctuations in smaller samples, and under the assumption that the model described by Equation 3 characterizes the distribution well, any deviations from zero should be entirely attributable to observational effects or measurement errors. I.e., in the large sample limit and adopting the assumptions of this exercise, μ should be equal to μ_{err} since the physical processes that are inducing the measured offsets, and thus dictate μ_{int}, should have no preferred directionality in our slits. Also note, that despite the high degree of degeneracy between σ_{err} and σ_{int}, the distributions of σ_{err} and σ_{int} across all Monte Carlo realizations do not appreciably overlap.

It is clear from this exercise that the result found in the previous section regarding the difference between the offsets of the lower- and higher-luminosity samples persists here. The two intrinsic spreads differ by $\sim 1.7\sigma$ ($\sigma_{int} = 0.53^{+0.17}_{-0.14}$ vs. $1.21^{+0.33}_{-0.37}$, respectively) and show the same directionality as the measured difference. This is perhaps not surprising given the similar distribution of errors for both samples, but it serves to lend credence to the inference made in the last section that offsets are generally larger in UV-brighter galaxies. Additionally, the 1σ confidence interval for σ_{err} for all three samples encompasses both our average formal uncertainty and zero, which suggests it is unlikely that there are additional hidden uncertainties in our data. The full distribution, unsurprisingly, shows a intrinsic distribution intermediate to the lower- and higher-luminosity samples ($\sigma_{int} = 0.78^{+0.19}_{-0.16}$). Note that in all three cases with the possible exception of the higher-luminosity sub-sample, the Gaussian parameterization does poorly at properly accounting for the large offset tail of the distribution.

In order to search for possible redshift evolution in the intrinsic distribution, we compare our recovered value of σ_{int} for the higher-luminosity sub-sample to a similar value computed by Hoag et al. (2019a) for galaxies in five independent redshift bins running from $3 \le z < 5.5$. The higher-luminosity sub-sample is chosen as a point of comparison because it contains galaxies with similar UV luminosities as those in Hoag et al. (2019a). While we do not adopt the complex forward-modeling approach of that work used to recover the intrinsic distribution, our recovered values still serves as a fair comparison under the assumption of azimuthal symmetry. Our estimated value of σ_{int}, though generally smaller than the equivalent

---

[12] From here on out we will refer to this distribution as "intrinsic" and ask the reader to keep in mind that it is still projected and one-dimensional and, thus, these intrinsic offsets are still lower limits to the true three-dimensional offsets.
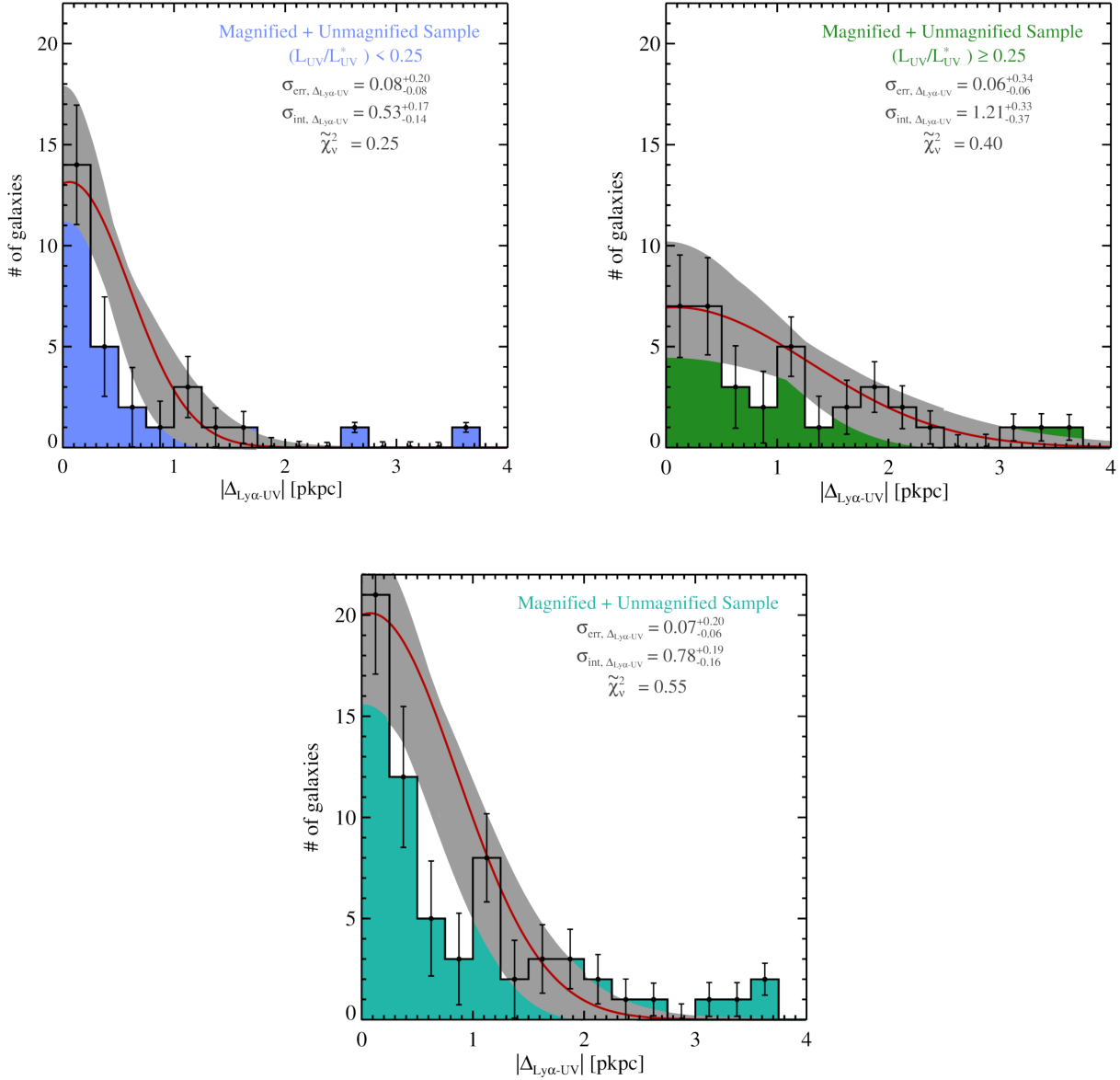
Figure 5. *Top Left:* Estimate of the instrinsic distribution of the one-dimensional projected Lyα-UV offsets ($\Delta_{Ly\alpha-UV,\,int}$) for the low-luminosity sample using the methodology described in §3.2. The solid histogram indicates the observed distribution of $\Delta_{Ly\alpha-UV}$, while the error bars show the effective 1σ spread across the 1000 Monte Carlo realizations used to estimate the intrinsic distribution. The shaded region indicates the effective 1σ spread of the convolved Gaussian best-fit (see Equation 3) to the observed distribution across all Monte Carlo realizations, while the solid red line indicates the median. The median values of the spread in the observed distribution resulting from the error (σ_{err}) and from astrophysically-induced offsets (σ_{int}), along with their effective 1σ bounds taken from the 16th/84th percentile of all realizations are shown in the upper right. The median reduced χ^2 of the best-fit models for all realizations is also shown. *Top Right:* Identical to the top left, but showing the results of this exercise for the higher-luminosity sample. *Bottom:* Identical to the other two panels, but done for the full sample.

values in Hoag et al. (2019a), differ from only their lowest-redshift measurement by $\gtrsim 3\sigma$. For the measurements of the remainder of the redshift bins the difference is $< 1\sigma$. From this perspective, there is also little evidence to suggest significant evolution in the intrinsic offset distribution as a function of redshift.

3.3 Explaining the Lyα-UV Offsets

Several potential scenarios could be invoked to explain the behavior of increasing offsets in increasingly UV bright galaxies. The first, and perhaps most obvious explanation, is that UV-brighter galaxies reside in more massive halos than their fainter counterparts (e.g., Mason et al. 2015), and, therefore are a more clustered population than their lower-luminosity counterparts (e.g., Durkalec et al. 2018). Under such a scenario, rather than witnessing true intragalaxy offsets, the offsets measured in our sample would predom-

inantly result from emission originating from multiple galaxies in close proximity with differing Lyα/UV luminosity ratios. However, as discussed in §2.4, this is unlikely to be the case as most of the galaxies in our sample are observed to be isolated systems, at least to the depth of our rest-frame UV imaging. For those systems where multiple components were observed, it appeared unlikely that the offset was due to the presence of multiple components (see, e.g., the left panel of Figure 2).

These considerations do not preclude late-stage merging activity as the genesis for at least some of the measured offsets, and future work searching for evidence of such activity in their rest-frame UV images would be necessary to make definitive claims. However, such late-stage merging activity would have difficulty in inducing the larger offsets observed in our sample and cannot explain those galaxies where Lyα appears to originate well away from the UV bright portions of the galaxy (see, e.g., both panels of Figure 2). This logic also applies for scenarios where violent disk instabilities (VDI; Mo et al. 1998; Genzel et al. 2008; Dekel et al. 2009; Inoue et al. 2016) induce large star-forming clumps that could, while being sub-dominant in the rest-frame UV, act as sites of copious Lyα production with little to no obscuring dust. Observational evidence of such UV-faint, Lyα-bright internal structure has, through lensing, been observed at high redshifts (see, e.g., Vanzella et al. 2017a,b, 2019). For more modest offsets, however, it seems possible, given that galaxy size appears to scale with the size of the offset, that structure internal to the galaxy, whether induced by VDIs or by merging activity, is the genesis for at least some of the offsets seen in this sample. Future analysis involving a more careful morphological analysis of the internal structure of these galaxies, as in, e.g., Ribeiro et al. (2017), would be needed to make definitive claims.

A final possibility related to merging activity is the presence of UV-faint or UV-dark Lyα-emitting galaxies (e.g., Bacon et al. 2015; Maseda et al. 2018; Mary et al. 2020) in a pre- or early-stage merging configuration. However, such systems are fairly rare, with number densities of $\sim 2 - 10 \times 10^{-5}$ Mpc^{-3} at $3 \lesssim z \lesssim 7$ from extremely deep MUSE observations, and have typical Lyα line luminosities approximately three times lower than that of our combined sample. As there is no correlation between intrinsic line luminosity and observed offset, i.e., offsets are not preferentially seen in galaxies with fainter $L_{Ly\alpha}$, it is unlikely that such galaxies are primarily responsible for the observed offsets.

A second set of scenarios involve Lyα emission from infalling or outflowing H I gas. A scenario involving inflowing gas follows that proposed by Rauch et al. (2011), in which a $z = 3.344$ galaxy is observed with a spectrum characteristic of a damped Lyα (DLA) system at a spatial location coincident with the broadband rest-frame UV emission and a spatially asymmetric Lyα emission that protrudes $\sim$20 kpc from the UV center, whose main component was observed to be offset at level comparable to the largest offsets observed in our sample. This galaxy, which has an *HST*/ACS *F*814*W* magnitude of $m_{F814W} = 26.3$ (Coe et al. 2006) translating to $L_{UV} \sim 0.3 L_{UV}^{*}$ assuming a beta slope of $\beta = -2$ and L_{UV}^{*} of Bouwens et al. (2015), has a UV brightness comparable to the median L_{UV} of our sample. Under the scenario proposed in that work, the gaseous halo was supposed to be split open by beamed ionizing radiation or other anisotropic process, or, alternatively, a part of the galaxy containing young stars might have been exposed through tidal interaction with an unseen companion. With the gas no longer being capable of resonantly scattering Lyα photons due to its removal or ionization, Lyα photons were free to propagate and scatter off of infalling filaments. Additionally, ionizing radiation is similarly able to escape through these channels

resulting in Lyα fluorescence off of infalling or nearby gas (see, e.g., Mas-Ribas & Dijkstra 2016). Such cavities are similarly suggested to induce Lyα and Lyman continuum escape in the rare class of Lyman continuum emitting galaxies observed at high redshifts (see, e.g., Shapley et al. 2016; Vanzella et al. 2016, 2018, 2020).

This phenomenon is potentially more likely to occur in the brighter sample due to the potential excess clustering, or, as we will discuss below, the potential for stronger stellar feedback. In addition, any activity due to an active galactic nuclei (AGN) could help facilitate and enhance this effect (e.g., Windhorst et al. 1998). While the Lyα emitting regions of the galaxies observed in our sample do not appear as large as those seen in Rauch et al. (2011), this lack does not necessarily preclude such a possibility. Deeper Lyα spectroscopy to observe the full spatial extent of the Lyα emitting region along with an estimate of the systemic redshift and, possibly, the nuclear activity of each galaxy through, e.g., the detection of the CIII] λ1907,1909Å doublet, HeII λ1640Å emission (e.g., Cassata et al. 2013), or, constraints on the systemic redshift the [CII] λ158μm transition (e.g., Pentericci et al. 2016; Bradač et al. 2017; Cassata et al. 2020) would be necessary to test this scenario more fully. Deep IFU data in which the astrometry is sufficiently precise to allow for the measurement of small offsets (e.g., Bacon et al. 2015) could be used as a basis for such a test if accompanied by measures of systemic redshifts through deep NIR spectroscopy or ALMA observations.

Alternatively, or in addition, anisotropic outflows due to stellar feedback could entrain Lyα photons, either through resonant scattering or fluorescence, or otherwise facilitate their escape from the galaxies by decreasing the covering fraction of H I gas through the opening of channels in the gaseous halo. It has been shown at $z \sim 1 - 2$ that, in lower-mass star-forming galaxies such as those studied here, stellar feedback is capable of altering the velocity structure of *in situ* gas (Hirtenstein et al. 2019; Pelliccia et al. 2020) especially for galaxies with the highest star-formation rates ($\mathcal{SFR}$). Additionally, pervasive large outflow velocities have been observed in $\sim L^{*}$ star-forming galaxies at $2 \lesssim z \lesssim 6$ devoid of AGN activity (e.g., Steidel et al. 2010; Talia et al. 2017; Sugahara et al. 2019; Ginolfi et al. 2020). Such outflows result in extended halos of chemically-enriched gas expelled from the galaxy (e.g., Fujimoto et al. 2020).

In order to estimate the average level of stellar feedback in the galaxies in our two sub-samples, we began by taking the median rest-frame UV absolute magnitude of our fainter and brighter sample, $M_{UV} = -18.33$ and -20.49, respectively, and converted them to an average $\mathcal{SFR}$ for each sample using the relation of Jaacks et al. (2012):

$$\log(\mathcal{SFR}) = -0.41 M_{UV} - 7.77 \qquad (4)$$

with a scatter of ~ 0.2 dex. This relation is derived from a suite of hydrodynamical simulations of galaxies at similar redshifts to those in our sample and is broadly consistent with estimates from a variety of observational works on high-redshift galaxies (e.g., de Barros et al. 2014; Faisst et al. 2020)[13] and yields values that, for the purposes of this exercise, do not meaningfully depart from more traditional estimates (Kennicutt 1998). This relation assumes

---

[13] While the level of concordance of the normalization with observational works depends on the exact star-formation history assumed, the slope of the Jaacks et al. (2012) relation is consistent with these works, which, for this exercise, is the relevant concern.

a stellar extinction of $E(B - V)_* = 0.1$ for all galaxies, a value consistent with estimates of the average dust extinction properties of high-redshift galaxies (e.g., Bouwens et al. 2012; Huang et al. 2016; Strait et al. 2020). The resultant average $\mathcal{SFR}$s are 0.6±0.3 and 4.3±1.9 $\mathcal{M}_\odot$ yr^{-1} for the fainter and brighter samples, respectively. Assuming outflow rates of atomic gas induced by stellar feedback scale linearly with $\mathcal{SFR}$ with only a mild stellar mass dependence (e.g., Fluetsch et al. 2019; Ginolfi et al. 2020, though see also Marchi et al. 2019 for an alternative view), the outflow rate in the brighter sample is ∼ 7.5× larger than the fainter sample. Similarly, under the assumption that the outflow velocity of atomic gas scales as $\sqrt{\mathcal{SFR}}$ with, again, only a weak dependence on stellar mass (e.g., Heckman et al. 2015; Cicone et al. 2016), the outflow velocity induced by stellar feedback in the brighter sample is ∼ 2.75× that of the fainter sample. While it is possible that dust content may increase with increasing UV-brightness for high-redshift galaxies, the increase is likely mild (e.g., Bouwens et al. 2011, 2014; Smit et al. 2012; Álvarez-Márquez et al. 2016; Khusanova et al. 2020), and would only serve to enhance this disparity. These more powerful outflows would have the potential to push more gas to larger galactocentric distances, allowing for the possibility of larger observed spatial offsets of fluorescing gas. In addition, if such outflows were anisotropic, the ionizing radiation would likely preferentially beam in the direction of the outflow, due to the lower covering fraction of neutral gas in that direction, which would result in a natural conduit through which to light the interface between the galaxy and its circumgalactic medium. The various relations used for this scenario, $M_{UV} - \mathcal{SFR}$, $\mathcal{SFR} - \dot{M}_{out}$, or $\mathcal{SFR} - v_{out}$, have been shown to not vary strongly as a function of redshift, satisfying the requirement that the evolution in the process or processes inducing the offsets must be mild or nonexistent over the redshift range $2 \le z \le 7$ (see §3.1).

Such scenario is also broadly consistent with the results presented in Ribeiro et al. (2020). In that study, the percentage of galaxies with considerable Lyα-UV offsets, classified as "Offset" emitters in that work, generally increased with increasing UV brightness (see their Figure 4) and the specific star formation rate of that class was, on average, the highest amongst all of the galaxy classes studied (though their $\mathcal{SFR}$ was statistically indistinguishable from the other classes). Additionally, while the velocity offset between systemic and the interstellar medium (ISM) lines was similar in the Offset class relative to all other LAEs analyzed in that work, the velocity offset between the systemic and the Lyα line was the largest in the Offset emitters, suggesting that the Lyα emission originated from backscattering off of outflowing gas or from an anisotropic gas distribution allowing for Lyα fluorescence from background gas in close proximity. Note again, however, while that study probed four magnitudes in UV brightness, the faintest galaxies in Ribeiro et al. (2020) would still be considered part of our brighter sub-sample, precluding a more comprehensive comparison.

3.4 Induced Slit Losses

While surveys of high-redshift LAEs are becoming common with grism observations (e.g., Pirzkal et al. 2004; Malhotra et al. 2005; Rhoads et al. 2009; Schmidt et al. 2014, 2016; Treu et al. 2015; Tilvi et al. 2016; Larson et al. 2018) and IFUs such as KCWI mounted on Keck II and MUSE mounted on the VLT Yepun Unit Telescope (e.g., Bacon et al. 2015, 2017; Karman et al. 2015; Richard et al. 2015; Lagattuta et al. 2017, 2019; Cai et al. 2018; Vanzella et al. 2020; Nielsen et al. 2020), the targeting of high-redshift candidates with slit spectrographs remains a common ob-

servational strategy to census the high-redshift universe. Further, modern IFU studies from MUSE, for all but those with the deepest observations, lack the the astrometric precision needed to reliably measure $|\Delta_{\text{Ly}\alpha-\text{UV}}|$ at the level observed in the samples presented in this paper (see, e.g., Urrutia et al. 2019). In a census of the high-redshift universe using slit spectroscopy, slits are almost always placed at the barycenter of the rest-frame continuum UV emission and integrated only long enough to detect galaxies if they have appreciable emission in Lyα (in the absence of other rest-frame UV emission lines). The resultant observations are used to derive the Lyα fraction at a fixed EW limit for various sub-samples of galaxies or to otherwise probe the Lyα properties of the observed population to make inferences on the evolution of galaxy properties and the properties of the intergalactic medium at early times (e.g., Ota et al. 2008; Pentericci et al. 2011; Stark et al. 2011; Treu et al. 2013; Tilvi et al. 2014; De Barros et al. 2017; Mason et al. 2018, 2019; Pentericci et al. 2018b; Hoag et al. 2019b; Fuller et al. 2020). As is discussed in detail in Hoag et al. (2019a), offsets between the UV and Lyα emission of target galaxies will, if severe, modulate the Lyα properties of the targeted population due to slit losses, which can, in turn, considerably modulate inferences on the nature of reionization.

In order to quantify such losses for our sample, we relied on identical simulations to those described in Lemaux et al. (2009). In these simulations, the Lyα halo is described by an exponential profile with $r_h = 0.2''$, roughly the average (circularized) size of the UV continuum for galaxies at this redshift (e.g., Venemans et al. 2005; Overzier et al. 2006; Ribeiro et al. 2016; Pentericci et al. 2018b). Note that none of the conclusions in this section change appreciably if we instead adopt the slightly smaller size characterized by the average measured r_e value in our sample (see §2.4). We will return to the case where the Lyα halo is considerably larger than the UV continuum later in the section. The simulated galaxies are well centered in a slit of length 10″, convolved with a Gaussian seeing kernel of varying sizes, and shifted along the minor axis in increments of 0.0125″. Slit widths are set to 1″, a typical width employed for FORS2/DEIMOS slits. The ratio between the light entering the slit and the total output of the galaxy, ω, is considered the slit throughput, with 1-ω defining the slit loss. For a seeing kernel of full width at half maximum equal to 0.8″, a typical value for Mauna Kea in the i band and also similar to the conditions required at Cerro Paranal for our bright sample, the slit loss only increases[14] by ∼2% for the average offset measured in our full sample, a negligible difference. This depreciation does not vary meaningfully if we use the average offset in the brighter or fainter samples observed in the previous section, nor if average projection effects are taken into account. It appears, as a whole, and differentially as a function of UV luminosity, the Lyα properties of our DEIMOS/FORS2 sample are largely unaffected by the average observed offsets.

However, for individual offsets, the increase in slit loss, even with the relatively wide DEIMOS slits, can be devastating if the offsets unfortuitously manifest perpendicular to the major (spatial) axis of the slit. For the largest offsets observed in our combined sample (∼3.5 kpc), offsets that are observed to varying degrees both in our fainter and brighter sample, additional slit losses exceed

---

[14] Here and throughout the section, unless noted otherwise, we are characterizing *additional* slit losses induced by the spatial offset between the UV and Lyα emission. We do not additionally consider the slit losses that already occur when the Lyα emission is perfectly centered in the slit along its minor axis (see, e.g., Lemaux et al. 2009 and Figure 6 for a characterization of absolute slit losses).
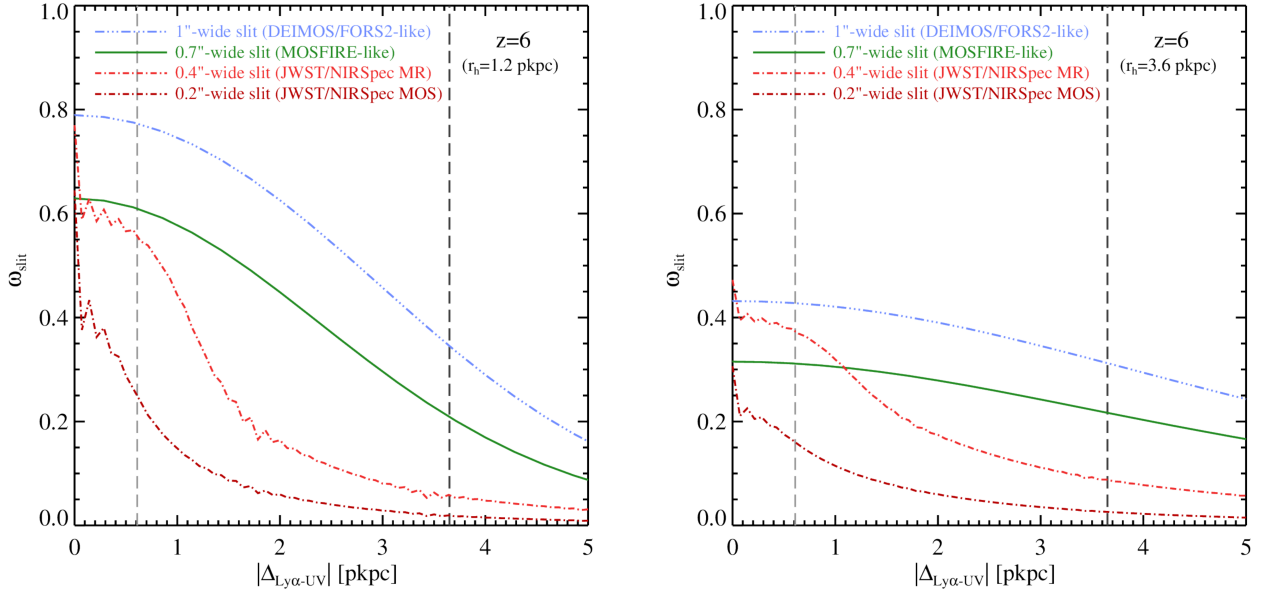
Figure 6. *Left:* Normalized slit throughput ($\omega_{slit} \equiv 1$-slit loss) of Lyα emission of a simulated LAE as a function of the Lyα-UV offset ($|\Delta_{Ly\alpha-UV}|$) for slit-spectroscopic observations using a variety of different instruments and telescopes. In each case, the slit is assumed to be placed directly on the UV barycenter along both axes and the offset is assumed to be perpendicular to the major axis. The simulation uses the methodology described in §3.4 and Lemaux et al. (2009). We adopt an exponential profile with $r_h = 1.2$ kpc to characterize the Lyα emission and translate the angular offset to physical ones assuming $z = 6$. The light blue dot-dashed and solid green lines indicate ω_{slit} as a function of $|\Delta_{Ly\alpha-UV}|$ for ground-based slit observations employing $1.0''$- and $0.7''$-wide slits, respectively, under $0.8''$ seeing. The orange and red dot-dashed lines show those values for *JWST*-NIRSpec medium resolution single slit and high-resolution multi-object spectroscopic observations, respectively. The light and dark vertical dashed lines indicate the average and maximum $|\Delta_{Ly\alpha-UV}|$ for our sample. *Right:* Indentical to the left panel, but the emitting region of Lyα is now assumed to be three times the UV size of the galaxy.

50% and increase to over 75% if average projection effects are taken into account. As such, it is clear that observations of large samples of galaxies at these redshifts are necessary to mitigate this stochasticity in order to draw robust conclusions about the nature of galaxy populations and reionization at these redshifts.

The above results remain broadly applicable for instruments that employ slightly smaller slit widths such as the Multi-Object Spectrograph for Infrared Exploration (MOSFIRE; McLean et al. 2012). For typical MOSFIRE slit widths, $0.7''$, the additional slit losses induced by the average offset in our sample are $\sim 5\%$, again a mostly negligible amount. However, large offsets, if perpendicular to the major axis of the slit, become an even larger hindrance, exceeding 70% even under the assumption of modest projection effects in our sample. These losses are further exacerbated in the case of targeted observations with the medium-resolution setting for the James Webb Space Telescope NIRSpec instrument, which employs $0.4''$-wide slits. For the *JWST*-NIRSpec simulations we do not convolve the simulated galaxy with an atmospheric seeing kernel, but rather were convolved with the NIRSpec *F110W* PSF generated by the PYTHON-based WEBBPSF[15] In such observations, while additional slit losses are only $\sim$10-15% for the average $|\Delta_{Ly\alpha-UV}|$ measured in our sample, the amount of Lyα entering the slit is severely reduced for the largest offsets observed in our sample, with > 90% additional slit losses when the offset is parallel to the slit

minor axis and $\sim$95% total slit loss. For large samples it will be important to account for this bias in order to properly quantify, e.g., Lyα escape fractions and to make inferences on kinematics from the Lyα line.

The situation gets more dire for multi-object NIRSpec spectroscopy (NIRSpec-MOS), which employs both narrower ($0.2''$) and shorter ($1.38''$) slits in its nominal mode. For such observations, even the relatively modest average $|\Delta_{Ly\alpha-UV}|$ measured in our sample results in additional slit losses of $\sim$60% (75% on an absolute scale) and slit losses approach complete at the largest offsets, with, *at minimum* 98% of the total Lyα flux lost for offsets perpendicular to the major axis of the slit. In the left panel of Figure 6, we plot the absolute slit losses as a function of $|\Delta_{Ly\alpha-UV}|$ for the two ground-based and two *JWST* cases presented above.

If we instead assume in these simulations that the Lyα halo is considerably larger than the average size of the UV continuum (as in, e.g., Wisotzki et al. 2016; Leclercq et al. 2017; Erb et al. 2018), the additional slit losses reported above are mitigated somewhat. For instance, if we assume that the half light radius of the Lya halo is three times that of the UV continuum, $r_{h, Ly\alpha} = 0.6''$, the additional slit loss drops to negligible levels[17]. However, in the case of the maximal offsets observed in our sample, *even in the case of larger Lyα halos, the additional slit losses reach 60-70% for JWST-NIRSpec MR observations* if the offsets are parallel to the minor axis of the slit. Similarly, *the slit losses remain near total for NIRSpec-MOS observations for galaxies with the largest offsets, with, at minimum, $\sim$97% of the total Lyα flux incident lost, and 85%*

---

[15] https://www.stsci.edu/jwst/science-planning/proposal-planning-toolbox/psf-simulation-tool tool. Additionally, we change the length of the slit in the simulation to $3.65''$, the nominal length for MR slit spectroscopy with NIRSpec[16], though, in practice, this makes no appreciable difference.

[17] Though, note that the larger halo increases *total* amount of slit loss due to the larger size relative to the slit aperture.

of total for the average observed offset. Clearly, regardless of the properties of the Lyα halos at high redshift, such offsets are crucial to quantify for observations of individual galaxies if the Lyα line is to be meaningfully used to place physical constraints.

4 CONCLUSIONS

In this paper, we analyzed the projected spatial offsets of the UV continuum and the Lyα emission for a sample of 36 high-redshift ($5 \lesssim z \lesssim 7$) lensed LAEs taken from Fuller et al. (2020) and 30 high-redshift non-lensed LAEs drawn from Pentericci et al. (2011) and Pentericci et al. (2018b). This sample spans more than three orders of magnitude in intrinsic UV brightness and represents the first such measurements performed on galaxies at these redshifts. The measured spatial offsets of these samples were compared internally for evidence of dependence on various physical parameters. A comparison was also made to a variety of lower-redshift samples compiled by Ribeiro et al. (2020), Hoag et al. (2019a), and Khusanova et al. (2020) to investigate the possible redshift evolution of these offsets over a broad baseline ($2 \lesssim z \lesssim 7$). Various scenarios were explored for the observed offsets and simulated spectroscopic observations employing slits of various sizes appropriate for ground-based and future space-based spectrographs were performed to estimate the loss of Lyα light induced by these offsets. We list our main conclusions below:

• While ~40% of the LAEs in our sample have observed UV continuum to Lyα projected spatial offsets, $|\Delta_{Ly\alpha-UV}|$, significant at the $\geq 3\sigma$, the median offset was found to be relatively modest, $|\widetilde{\Delta}_{Ly\alpha-UV}| = 0.61 \pm 0.08$ kpc.

• A small fraction of our sample, ~10%, exhibited Lyα offsets of ≥ 2 kpc, and the largest Lyα offsets were observed nearly 4 kpc from the UV barycenters.

• Within our own sample, and in comparisons to large samples of lower-redshift LAEs, no significant evolution was observed in $|\Delta_{Ly\alpha-UV}|$ as a function of redshift over the redshift range $2 \lesssim z \lesssim 7$.

• Splitting our sample into UV-brighter ($\widetilde{L_{UV}}/L^*_{UV} = 0.67$) and UV-fainter ($\widetilde{L_{UV}}/L^*_{UV} = 0.10$) sub-samples, a significant difference was observed in $|\Delta_{Ly\alpha-UV}|$, with UV-brighter galaxies exhibiting offsets ~3× larger than their UV-fainter counterparts (0.89 ± 0.18 vs. 0.27 ± 0.05 kpc, respectively). Despite the heterogeneous selection methods and the complications of lensing differentially affecting the primary constituents of the two sub-samples, we found this difference to persist at the $\gtrsim 2-3\sigma$ level through a variety of complementary approaches to measuring the disparity in the offsets. As such, we argued that the differences observed in $|\Delta_{Ly\alpha-UV}|$ between these samples represent a true difference rather than an artifact of the differing observing strategies, measurements, or lensing effects. A reasonably strong positive correlation was also observed between $|\Delta_{Ly\alpha-UV}|$ and the intrinsic UV half-light radii of galaxies in our sample.

• A variety of scenarios were discussed to explain the larger observed offsets in the brighter sample. Merging was found to be an unlikely cause, though it is possible or even likely that late-stage merging activity and violent disk instabilities could be responsible for some of the modest offsets observed in our sample. Scenarios involving Lyα fluorescence and/or backscattering appeared the most consistent with the observations, especially for those galaxies where the $|\Delta_{Ly\alpha-UV}|$ exceeded their UV size.

• From mock spectroscopic observations it was shown that the relatively small average $|\Delta_{Ly\alpha-UV}|$ offsets observed in our sample resulted in small additional slit losses (~2%) for a DEIMOS-like setup with 1″-wide slits, losses which did not meaningfully change if we instead used those average offsets measured at other redshifts or for the brighter or fainter sub-samples. Employing smaller slit widths, e.g., a MOSFIRE-like 0.7″-wide slit or a *JWST*-NIRSpec-like single 0.4″-wide slit, only increased the average additional slit losses moderately (~5-15%). However, for galaxies observed with a nominal *JWST*-NIRSpec MOS setup, with slit sizes of 0.2″×1.38″, even the relatively modest average offsets have a large effect, with slit losses increasing ~60%. Further, galaxies with the largest observed offsets were found to have their Lyα line fluxes depreciated $\gtrsim 70\%$ for 0.7-1′-wide slits in cases where the offset is perpendicular to the major axis of the slit. For 0.2″- and 0.4″-wide slits, such offsets would cause a >95% loss of flux, which effectively renders Lyα unobservable for all but the brightest galaxies if mitigating measures are not taken. Both slitless and IFU observations will be crucial to contextualize these observations on an individual and statistical level.

Given the relatively small average offsets observed over a large redshift baseline, it is unlikely that inferences on the Epoch of Reionization using the LAE fraction or other observed properties of Lyα (e.g., Mason et al. 2018; Hoag et al. 2019b) are altered meaningfully by these offsets as long as the samples used are large enough. However, in smaller samples or studies of individual galaxies, it is clear that such offsets can have a severe deleterious effect on attempts at accurately measuring Lyα properties. While the ability to measure rest-frame optical emission lines in galaxies at the Epoch of Reionization will come with the launch of *JWST*, the Lyα properties of such galaxies will still be crucial to constrain considerable aspects of both the internal physics of galaxies and that of their surrounding medium. As such, care must be taken to quantify UV-Lyα offsets properly and account for them in either the observational strategy or mitigate the confusion they induce when making inferences on such populations.

which is operated by the Jet Propulsion Laboratory, California Institute of Technology under a contract with NASA. Some portion of the spectrographic data presented herein was based on observations obtained with the European Southern Observatory Very Large Telescope, Paranal, Chile. The remainder of the spectrographic data presented herein were obtained at the W.M. Keck Observatory, which is operated as a scientific partnership among the California Institute of Technology, the University of California, and the National Aeronautics and Space Administration. The Observatory was made possible by the generous financial support of the W.M. Keck Foundation. We thank the indigenous Hawaiian community for allowing us to be guests on their sacred mountain, a privilege, without which, this work would not have been possible. We are most fortunate to be able to conduct observations from this site.

DATA AVAILABILITY

The data used in this study will be shared upon reasonable request to the corresponding author.

REFERENCES

Abell G. O., Corwin Harold G. J., Olowin R. P., 1989, ApJS, 70, 1
Álvarez-Márquez J., et al., 2016, A&A, 587, A122
Appenzeller I., et al., 1998, The Messenger, 94, 1
Arnouts S., D'Odorico S., Cristiani S., Zaggia S., Fontana A., Giallongo E., 1999, A&A, 341, 641
Bacon R., et al., 2010, The MUSE second-generation VLT instrument. p. 773508, doi:10.1117/12.856027
Bacon R., et al., 2014, The Messenger, 157, 13
Bacon R., et al., 2015, A&A, 575, A75
Bacon R., et al., 2017, A&A, 608, A1
Becker R. H., et al., 2001, AJ, 122, 2850
Bertin E., 2011, in Evans I. N., Accomazzi A., Mink D. J., Rots A. H., eds, Astronomical Society of the Pacific Conference Series Vol. 442, Astronomical Data Analysis Software and Systems XX. p. 435
Bertin E., Arnouts S., 1996, A&AS, 117, 393
Béthermin M., et al., 2020, A&A, 643, A2
Bouwens R. J., et al., 2011, ApJ, 737, 90
Bouwens R. J., et al., 2012, ApJ, 754, 83
Bouwens R. J., et al., 2014, ApJ, 793, 115
Bouwens R. J., et al., 2015, ApJ, 803, 34
Bradač M., Schneider P., Lombardi M., Erben T., 2005, A&A, 437, 39
Bradač M., et al., 2009, ApJ, 706, 1201
Bradač M., et al., 2014, ApJ, 785, 108
Bradač M., et al., 2017, ApJ, 836, L2
Bunker A. J., Moustakas L. A., Davis M., 2000, ApJ, 531, 95
Cai Z., et al., 2018, ApJ, 861, L3
Capak P. L., et al., 2015, Nature, 522, 455
Carniani S., et al., 2017, A&A, 605, A42
Caruana J., Bunker A. J., Wilkins S. M., Stanway E. R., Lorenzoni S., Jarvis M. J., Ebert H., 2014, MNRAS, 443, 2831
Caruana J., et al., 2018, MNRAS, 473, 30
Cassata P., et al., 2013, A&A, 556, A68
Cassata P., et al., 2015, A&A, 573, A24
Cassata P., et al., 2020, A&A, 643, A6
Castellano M., et al., 2010, A&A, 524, A28
Cicone C., Maiolino R., Marconi A., 2016, A&A, 588, A41
Coe D., Benítez N., Sánchez S. F., Jee M., Bouwens R., Ford H., 2006, AJ, 132, 926
Curtis-Lake E., et al., 2016, MNRAS, 457, 440
Dawson S., Spinrad H., Stern D., Dey A., van Breugel W., de Vries W., Reuland M., 2002, ApJ, 570, 92
Dayal P., Maselli A., Ferrara A., 2011, MNRAS, 410, 830
De Barros S., et al., 2017, A&A, 608, A123
Dekel A., Sari R., Ceverino D., 2009, ApJ, 703, 785
Dijkstra M., 2014, Publ. Astron. Soc. Australia, 31, e040

Dijkstra M., Mesinger A., Wyithe J. S. B., 2011, MNRAS, 414, 2139
Dijkstra M., Gronke M., Venkatesan A., 2016, ApJ, 828, 71
Durkalec A., et al., 2018, A&A, 612, A42
Ebeling H., Edge A. C., Henry J. P., 2001, ApJ, 553, 668
Erb D. K., Steidel C. C., Chen Y., 2018, The Kinematics of Extended Lyα Emission in a Low-mass, Low-metallicity Galaxy at z = 2.3 (arXiv:1807.00065), doi:10.3847/2041-8213/aacff6
Faber S. M., et al., 2003, in Iye M., Moorwood A. F. M., eds, Society of Photo-Optical Instrumentation Engineers (SPIE) Conference Series Vol. 4841, Instrument Design and Performance for Optical/Infrared Ground-based Telescopes. pp 1657–1669, doi:10.1117/12.460346
Faisst A. L., et al., 2020, ApJS, 247, 61
Fan X., et al., 2006, AJ, 132, 117
Fazio G. G., et al., 2004, ApJS, 154, 10
Ferkinhoff C., Hailey-Dunsheath S., Nikola T., Parshley S. C., Stacey G. J., Benford D. J., Staguhn J. G., 2010, ApJ, 714, L147
Finkelstein S. L., et al., 2011, ApJ, 735, 5
Fluetsch A., et al., 2019, MNRAS, 483, 4586
Fontana A., D'Odorico S., Poli F., Giallongo E., Arnouts S., Cristiani S., Moorwood A., Saracco P., 2000, AJ, 120, 2206
Fontana A., et al., 2010, ApJ, 725, L205
Ford H. C., et al., 1998, in Bely P. Y., Breckinridge J. B., eds, Proc. SPIE Vol. 3356, Space Telescopes and Instruments V. pp 234–248
Fujimoto S., et al., 2020, ApJ, 900, 1
Fukugita M., Ichikawa T., Gunn J. E., Doi M., Shimasaku K., Schneider D. P., 1996, AJ, 111, 1748
Fuller S., et al., 2020, ApJ, 896, 156
Fynbo J. U., Møller P., Thomsen B., 2001, A&A, 374, 443
Gardner J. P., et al., 2006, Space Sci. Rev., 123, 485
Genzel R., et al., 2008, ApJ, 687, 59
Gilmozzi R., Spyromilio J., 2007, The Messenger, 127, 11
Ginolfi M., et al., 2020, A&A, 633, A90
Grogin N. A., et al., 2011, ApJS, 197, 35
Guaita L., et al., 2015, A&A, 576, A51
Guaita L., et al., 2017, A&A, 606, A19
Hashimoto T., et al., 2018, Nature, 557, 392
Hashimoto T., et al., 2019a, PASJ, 71, 71
Hashimoto T., Inoue A. K., Tamura Y., Matsuo H., Mawatari K., Yamaguchi Y., 2019b, PASJ, 71, 109
Hayes M., Schaerer D., Östlin G., Mas-Hesse J. M., Atek H., Kunth D., 2011, ApJ, 730, 8
Heckman T. M., Alexandroff R. M., Borthakur S., Overzier R., Leitherer C., 2015, ApJ, 809, 147
Hirtenstein J., et al., 2019, ApJ, 880, 54
Hoag A., et al., 2019a, MNRAS, 488, 706
Hoag A., et al., 2019b, ApJ, 878, 12
Hoaglin D. C., Mosteller F., Tukey J. W., 1983, Understanding robust and exploratory data anlysis
Hu W., et al., 2017, ApJ, 845, L16
Huang K.-H., et al., 2016, ApJ, 817, 11
Inoue S., Dekel A., Mandelker N., Ceverino D., Bournaud F., Primack J., 2016, MNRAS, 456, 2052
Jaacks J., Nagamine K., Choi J. H., 2012, MNRAS, 427, 403
Johns M., et al., 2012, in Proc. SPIE. p. 84441H, doi:10.1117/12.926716
Karman W., et al., 2015, A&A, 574, A11
Kawamata R., Ishigaki M., Shimasaku K., Oguri M., Ouchi M., Tanigawa S., 2018, ApJ, 855, 4
Kennicutt Jr. R. C., 1998, ARA&A, 36, 189
Khusanova Y., et al., 2020, A&A, 634, A97
Koekemoer A. M., et al., 2011, ApJS, 197, 36
Kusakabe H., et al., 2020, A&A, 638, A12
Lagattuta D. J., et al., 2017, MNRAS, 469, 3946
Lagattuta D. J., et al., 2019, MNRAS, 485, 3738
Larson R. L., et al., 2018, ApJ, 858, 94
Le Fèvre O., et al., 2003, in Iye M., Moorwood A. F. M., eds, Proc. SPIE Vol. 4841, Instrument Design and Performance for Optical/Infrared Ground-based Telescopes. pp 1670–1681, doi:10.1117/12.460959
Le Fèvre O., et al., 2015, A&A, 576, A79

Le Fèvre O., et al., 2019, A&A, 625, A51
Le Fèvre O., et al., 2020, A&A, 643, A1
Leclercq F., et al., 2017, A&A, 608, A8
Lehnert M. D., Bremer M., 2003, ApJ, 593, 630
Lemaux B. C., et al., 2009, ApJ, 700, 20
Lemaux B. C., et al., 2018, A&A, 615, A77
Loiacono F., et al., 2021, A&A, 646, A76
Lotz J. M., et al., 2017, ApJ, 837, 97
MacKenty J. W., Kimble R. A., O'Connell R. W., Townsend J. A., 2008, Wide Field Camera 3: science capabilities and plans for flight operation. p. 70101F, doi:10.1117/12.790039
Malhotra S., et al., 2005, ApJ, 626, 666
Marchi F., et al., 2018, A&A, 614, A11
Marchi F., et al., 2019, A&A, 631, A19
Mary D., Bacon R., Conseil S., Piqueras L., Schutz A., 2020, A&A, 635, A194
Mas-Ribas L., Dijkstra M., 2016, ApJ, 822, 84
Maseda M. V., et al., 2018, ApJ, 865, L1
Mason C. A., Gronke M., 2020, MNRAS, 499, 1395
Mason C. A., Trenti M., Treu T., 2015, ApJ, 813, 21
Mason C. A., Treu T., Dijkstra M., Mesinger A., Trenti M., Pentericci L., de Barros S., Vanzella E., 2018, ApJ, 856, 2
Mason C. A., et al., 2019, MNRAS, 485, 3947
Mawatari K., et al., 2020, ApJ, 889, 137
McLean I. S., et al., 2012, in Ground-based and Airborne Instrumentation for Astronomy IV. p. 84460J, doi:10.1117/12.924794
McLure R. J., et al., 2018, MNRAS, 479, 25
Mo H. J., Mao S., White S. D. M., 1998, MNRAS, 295, 319
Morrissey P., et al., 2018, ApJ, 864, 93
Müller J. W., 2000, Journal of Research of the NIST, 105, 551
Nakajima K., et al., 2018, A&A, 612, A94
Nielsen N. M., Kacprzak G. G., Pointon S. K., Murphy M. T., Churchill C. W., Davé R., 2020, ApJ, 904, 164
Oke J. B., Gunn J. E., 1983, ApJ, 266, 713
Ono Y., et al., 2012, ApJ, 744, 83
Ota K., et al., 2008, ApJ, 677, 12
Overzier R. A., et al., 2006, ApJ, 637, 58
Partridge R. B., Peebles P. J. E., 1967, ApJ, 147, 868
Paulino-Afonso A., et al., 2018, MNRAS, 476, 5479
Peebles P. J. E., 1993, Principles of Physical Cosmology
Pelliccia D., et al., 2020, ApJ, 896, L26
Pelliccia D., et al., 2021, ApJ, 908, L30
Pentericci L., et al., 2011, ApJ, 743, 132
Pentericci L., et al., 2016, ApJ, 829, L11
Pentericci L., et al., 2018a, A&A, 616, A174
Pentericci L., et al., 2018b, A&A, 619, A147
Pirzkal N., et al., 2004, ApJS, 154, 501
Planck Collaboration et al., 2016, A&A, 596, A108
Planck Collaboration et al., 2020, A&A, 641, A6
Postman M., et al., 2012, ApJS, 199, 25
Rauch M., Becker G. D., Haehnelt M. G., Gauthier J.-R., Ravindranath S., Sargent W. L. W., 2011, MNRAS, 418, 1115
Rhoads J. E., et al., 2009, ApJ, 697, 942
Ribeiro B., et al., 2016, A&A, 593, A22
Ribeiro B., et al., 2017, A&A, 608, A16
Ribeiro B., et al., 2020, arXiv e-prints, p. arXiv:2007.01322
Richard J., et al., 2015, MNRAS, 446, L16
Ryan R. E. J., et al., 2014, ApJ, 786, L4
Sanders G. H., 2013, Journal of Astrophysics and Astronomy, 34, 81
Sawicki M., et al., 2008, ApJ, 687, 884
Schaerer D., Verhamme A., 2008, A&A, 480, 369
Schenker M. A., Ellis R. S., Konidaris N. P., Stark D. P., 2014, ApJ, 795, 20
Schmidt K. B., et al., 2014, ApJ, 782, L36
Schmidt K. B., et al., 2016, ApJ, 818, 38
Shapley A. E., Steidel C. C., Strom A. L., Bogosavljević M., Reddy N. A., Siana B., Mostardi R. E., Rudie G. C., 2016, ApJ, 826, L24
Shibuya T., Ouchi M., Nakajima K., Yuma S., Hashimoto T., Shimasaku K., Mori M., Umemura M., 2014, ApJ, 785, 64
Shibuya T., Ouchi M., Harikane Y., 2015, ApJS, 219, 15
Shibuya T., Ouchi M., Harikane Y., Nakajima K., 2019, ApJ, 871, 164
Smit R., Bouwens R. J., Franx M., Illingworth G. D., Labbé I., Oesch P. A., van Dokkum P. G., 2012, ApJ, 756, 14
Smit R., et al., 2018, Nature, 553, 178
Sobral D., Santos S., Matthee J., Paulino-Afonso A., Ribeiro B., Calhau J., Khostovan A. A., 2018, MNRAS, 476, 4725
Spergel D., et al., 2015, arXiv e-prints, p. arXiv:1503.03757
Stark D. P., Ellis R. S., Ouchi M., 2011, ApJ, 728, L2
Stark D. P., et al., 2015a, MNRAS, 450, 1846
Stark D. P., et al., 2015b, MNRAS, 454, 1393
Steidel C. C., Erb D. K., Shapley A. E., Pettini M., Reddy N., Bogosavljević M., Rudie G. C., Rakic O., 2010, ApJ, 717, 289
Steidel C. C., Bogosavljević M., Shapley A. E., Kollmeier J. A., Reddy N. A., Erb D. K., Pettini M., 2011, ApJ, 736, 160
Steidel C. C., Bogosavljević M., Shapley A. E., Reddy N. A., Rudie G. C., Pettini M., Trainor R. F., Strom A. L., 2018, ApJ, 869, 123
Strait V., et al., 2020, ApJ, 888, 124
Sugahara Y., Ouchi M., Harikane Y., Bouché N., Mitchell P. D., Blaizot J., 2019, ApJ, 886, 29
Talia M., et al., 2017, MNRAS, 471, 4527
Tamura Y., et al., 2019, ApJ, 874, 27
Teague R., Foreman-Mackey D., 2018, Research Notes of the American Astronomical Society, 2, 173
Tilvi V., et al., 2014, ApJ, 794, 5
Tilvi V., et al., 2016, ApJ, 827, L14
Tilvi V., et al., 2020, ApJ, 891, L10
Treu T., Schmidt K. B., Trenti M., Bradley L. D., Stiavelli M., 2013, ApJ, 775, L29
Treu T., et al., 2015, ApJ, 812, 114
Urrutia T., et al., 2019, A&A, 624, A141
Vanzella E., et al., 2016, ApJ, 825, 41
Vanzella E., et al., 2017a, MNRAS, 467, 4304
Vanzella E., et al., 2017b, ApJ, 842, 47
Vanzella E., et al., 2018, MNRAS, 476, L15
Vanzella E., et al., 2019, MNRAS, 483, 3618
Vanzella E., et al., 2020, MNRAS, 494, L81
Venemans B. P., et al., 2005, A&A, 431, 793
Verhamme A., Schaerer D., Atek H., Tapken C., 2008, A&A, 491, 89
Verhamme A., Orlitová I., Schaerer D., Hayes M., 2015, A&A, 578, A7
Verhamme A., Orlitová I., Schaerer D., Izotov Y., Worseck G., Thuan T. X., Guseva N., 2017, A&A, 597, A13
Westra E., et al., 2005, A&A, 430, L21
Windhorst R. A., Keel W. C., Pascarelle S. M., 1998, ApJ, 494, L27
Wisotzki L., et al., 2016, A&A, 587, A98
Wisotzki L., et al., 2018, Nature, 562, 229
Zheng Z., Cen R., Weinberg D., Trac H., Miralda-Escudé J., 2011, ApJ, 739, 62
Zheng Z.-Y., et al., 2017, ApJ, 842, L22
Zhou L., et al., 2020, A&A, 642, A155
de Barros S., Schaerer D., Stark D. P., 2014, A&A, 563, A81

APPENDIX A: CORRECTIONS FOR DIFFERENTIAL ATMOSPHERIC REFRACTION

In §2.1.1 it was discussed that a correction to the observed Lyα position for our magnified sample was required to account for the effects of differential atmospheric refraction (DAR). We describe that DAR correction here as well as DAR and astrometric effects on the estimate of the UV location of galaxies in our magnified sample.

For each mask that contained a LAE candidate used in our final sample, we compiled all slits that contained filler targets, typically potential cluster members, with apparent magnitudes[18]

---

[18] These slits were typically outside the *HST* coverage. While for such slits

brighter than $m_{AB} < 22.5$. For every such target on a given mask, the two dimensional spectrum was collapsed along the spectral axis in eight individual mostly airglow-free 40Å-wide windows running from ~6600Å to ~ 9700Å. For a given target, the spatial centroid was measured using the Gaussian fit method described above in each of the windows where the spectrum was defined, with typical centroid uncertainties being smaller than 1/10th of a pixel. This process was visually supervised and any windows with strong artifacts, astrophysical issues (e.g., an emission line appearing in a window), or other issues that prevented the spatial location from being measured robustly were excised. For all remaining windows, a first-order polynomial was fit to the object location vs. the central wavelength of the window using least-squares. Then, for each mask, the first-order term (i.e., slope) was averaged for all bright objects on that mask in order to parameterize the movement due to DAR as a function of wavelength. Between one and 49 bright objects per mask, with an average of 12, were used in this process. Despite our observations being extremely red for optical data, this correction could be somewhat large relative to the effect we are attempting to measure, with typical slopes of $\sim 3 \times 10^{-4}$ pix Å^{-1}. Finally, the raw Lyα spatial location for a candidate on a given mask was corrected using the measured slope and the difference between the Lyα wavelength and that of the central wavelength. Note that the formal uncertainty in the slope in all cases is dominated by other sources of error and is not included in our final error budget.

A second DAR issue arises when attempting to estimate the UV location of the magnified sample, as none of the galaxies in the magnified sample had sufficiently strong continuum in the DEIMOS observations. As discussed in §2.1.2, the DEIMOS design software, DSIM, provides a predicted location of an object at the central wavelength of the observations. However, the true location of an object can differ slightly due to observations being taken under different conditions and at different times than those used to generate the design file. In order to test the magnitude of this difference, we compared the predicted object location, called "CAT_OBJP" in the header of the SPEC2D data products, with the measured spatial centroid of each of the ~400 bright objects as described in §2.1.1. This spatial centroid was estimated at the spectral window that most closely matches that of the central wavelength of the mask on which a bright object was observed. After accounting for an indexing issue that causes CAT_OBJP to overestimate the pixel location by ~1 pixel, the median of the difference between CAT_OBJP and the measured location was zero with a normalized median absolute deviation (NMAD; Hoaglin et al. 1983) scatter of ~ 1.5 pixels[19]. The UV location for each candidate was then set to the index-corrected CAT_OBJP value.

For the three candidates that were in our sample that were not targeted but which were fortuitously subtended by one of our slits ("secondaries" adopting the terminology of Fuller et al. 2020), the UV object location is not estimated by the mask design software. In order to estimate a UV location that is methodologically consistent, we first estimated the location of the secondary from its (α, δ) in the ASTRODEEP catalog. This value was then corrected to an equivalent CAT_OBJP by using the median of the offset between CAT_OBJP and the location estimate using the α/δ of all targets on

a given mask. This equivalent CAT_OBJP was then treated the same as the CAT_OBJP values for the targeted candidates. An additional consideration in this process is the precision of the astrometry for all targets and secondaries, as any issues with the astrometry will manifest themselves in the expected location of the candidate galaxy. However, comparing our original design α/δ values for all targeted bright objects ($m_{AB} < 22$) across all fields to astrometric standards (e.g., GAIA2, SDSS, USNO), the NMAD scatter in α/δ is $\sim 0.04''$, small enough to ignore for this analysis.

APPENDIX B: ALTERNATIVE METHODOLOGY TO INFER THE INTRINSIC 1D OFFSET DISTRIBUTION

In this Appendix we adopt an alternative approach to inferring the intrinsic distribution of $\Delta_{Ly\alpha-UV}$ to that used in §3.2. As in §3.2, while we will refer to this distribution as intrinsic, we remind the reader that the values are still one-dimensional and projected, and thus represent a lower limit to the true three-dimensional offsets. For this calculation we again assume that the underlying distribution can be characterized by a convolution of two Gaussians, one with spread σ_{err} resulting from errors in the observation, measurement, and analysis processes, and one with spread σ_{int} resulting from astrophysically-induced offsets. In this approach, we estimate the likelihood of given σ_{int} for all measurements of a given sample by:

$$\mathcal{L}(\sigma_{int}) = \sum_{j=1}^{N} \frac{1}{\sqrt{2\pi}\sqrt{\sigma_{\Delta_{Ly\alpha-UV,j}}^2 + \sigma_{int}^2}}$$

$$e^{\frac{-(\Delta_{Ly\alpha-UV})^2}{2(\sigma_{\Delta_{Ly\alpha-UV},j}^2 + \sigma_{int}^2)}} \quad \text{(B1)}$$

where $\Delta_{Ly\alpha-UV,j}$ is the jth measurement of the Lyα-UV offset and $\sigma_{\Delta_{Ly\alpha-UV},j}$ is its associated uncertainty. Note that unlike the approach in §3.2, we do not fit for σ_{err}, but rather use the estimated uncertainties of each $\Delta_{Ly\alpha-UV}$ measurement. This likelihood is calculated for a finely-gridded array of σ_i values running from $0 \le \Delta_{Ly\alpha-UV} \le 4$ for each sample. The resultant likelihood distributions on σ_i are shown in Figure B1 for the full, lower-luminosity, and higher-luminosity samples along with the median values and the 16th/84th percentiles representing the effective 1σ bounds of the distribution. The resultant values, while systematically larger than those in §3.2, are statistically consistent with the values measured with the method in that section for each sample. As in other analyses, we find that the most likely σ_{int} value using this method for the lower-luminosity sample ($\sigma_{int} = 0.82^{+0.16}_{-0.13}$) is lower than that of their higher-luminosity counterparts ($\sigma_{int} = 1.43^{+0.20}_{-0.17}$) formally at the ~2.5$\sigma$ level, with very little overlap seen in the two likelihood distributions. The value for the higher-luminosity sample is now well in line with those measured by Hoag et al. (2019a) at all redshifts save their lowest redshift measurement, again suggesting little to no redshift evolution of $\Delta_{Ly\alpha-UV}$ for such galaxies.

---

the magnitudes were measured on a wide variety of observations across the different fields, these magnitudes were typically measured on some form of *R*- or *I*-band images.

[19] While the scatter here could be thought of as a systematic uncertainty, none of the main conclusions of this paper are meaningfully changed if we use a per-mask correction to the UV spatial location.
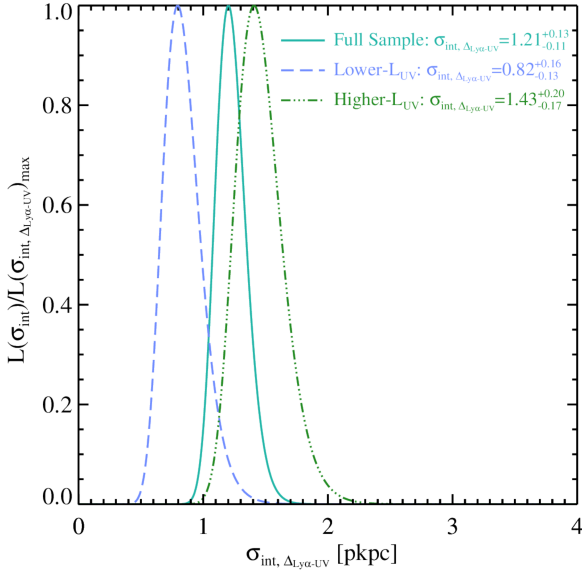
Affiliations:
[1]Department of Physics and Astronomy, University of California, Davis, One Shields Ave, Davis, CA 95616, USA
[2]INAF–Osservatorio Astronomico di Roma, via di Frascati 33, I-00040, Monte Porzio Catone, Italy
[3]Department of Physics and Astronomy, UCLA, Los Angeles, CA,

Figure B1. Likelihood distribution of the intrinsic projected one-dimensional spread of $\Delta_{\mathrm{Ly}\alpha-\mathrm{UV}}$ for the full (solid teal), lower-luminosity (dashed light blue), and higher-luminosity (dot-dashed green) samples. The the likelihood is calculated by the expression given in Equation B1. The median of the likelihood distribution for each sample along with their corresponding effective 1σ confidence interval is shown in the top right. As in other analyses, offsets are found to be significantly higher for galaxies that are brighter in the UV.

90095-1547, USA

[4]W. M. Keck Observatory, 65-1120 Mamalahoa Hwy, Kamuela, HI 96743, USA

[5]Harvard-Smithsonian Center for Astrophysics, 60 Garden St, Cambridge, MA, 02138, USA

[6]Hubble Fellow

[7]UCO/Lick Observatory, Department of Astronomy & Astrophysics, UCSC, 1156 High Street, Santa Cruz, CA, 95064, USA

[8]Leiden Observatory, Leiden University, PO Box 9513, 2300 RA Leiden, The Netherlands

[9]Space Telescope Science Institute, 3700 San Martin Drive, Baltimore, MD 21218, USA

[10]Leibniz-Institut für Astrophysik Potsdam (AIP), An der Sternwarte 16, 14482 Potsdam, Germany

[11]INAF - Osservatorio di Astrofisica e Scienza dello Spazio di Bologna, via Gobetti 93/3 - 40129 Bologna - Italy

[12]Max-Planck-Institut für Astronomie, Königstuhl 17, 69117 Heidelberg, Gemany

[13]Aix Marseille Université, CNRS, LAM (Laboratoire d'Astrophysique de Marseille) UMR 7326, 13388, Marseille, France

[14]Núcleo de Astronomía, Facultad de Ingeniería, Universidad Diego Portales, Av. Ejército 441, Santiago, Chile

[15]Scientific Support Office, Directorate of Science and Robotic Exploration, European Space Research and Technology Centre (ESA/ESTEC), Keplerlaan 1, 2201 AZ Noordwijk, The Netherlands

This paper has been typeset from a TEX/LATEX file prepared by the author.